SILICATE AND OXIDE MINERAL AND ISOTOPE GEOCHEMISTRY AS MONITORS OF FLUID CHEMISTRY IN DISTRICT-SCALE METASOMATIC PROCESSES, EASTERN SUCCESSION, MT ISA BLOCK

SILICATE AND OXIDE MINERAL AND ISOTOPE GEOCHEMISTRY AS MONITORS OF FLUID CHEMISTRY IN DISTRICT-SCALE METASOMATIC PROCESSES, EASTERN SUCCESSION, MT ISA BLOCK

6.1 INTRODUCTION

In a number of Fe-oxide Cu-Au districts, an association between widespread Na-(Ca) alteration, and more localised (K)-Fe alteration has been noted for several years (Hitzman et al., 1992; de Jong and Williams, 1995; Barton and Johnson, 1996; Frietsch et al., 1997; Pollard, 2001). However, the origins of metasomatic fluids, salt, sulphur and metals, as well as the role of regional-scale alteration in Cu-Au mineralisation processes remain contentious in these hydrothermal systems. In the Cloncurry District of the Proterozoic Mt Isa Block, crystallising plutons are the preferred source of saline fluids for both widespread sodic-(calcic) alteration and ore proximal (K)-(Fe) alteration (e.g. de Jong and Williams, 1995; Mark and Foster, 2000; Perring et al. 2000; Pollard, 2001), with supporting evidence having been drawn from stable isotopes, fluid inclusion data, and textural observations from magmatic-hydrothermal interface rocks at several locales. Variations in mineral assemblages between regional Na-(Ca)-rich and ore-proximal (K)-(Fe)-rich associations have been attributed to unmixing of H_2O-CO_2-NaCl $\pm$ $CaCl_2$-KCl fluids in response to temperature and/or pressure drops (Pollard, 2001) and/or to progressive enrichment of KCl and FeCl fluid concentrations due to leaching of these components during Na-(Ca) alteration (Oliver et al., in revision).

If crystallising plutons indeed acted as primary fluid sources for regional Na-(Ca) and ore-proximal (K)-(Fe) alteration, then it should be possible to track changes in isotopic and chemical signatures of metasomatic minerals from within the intrusions down temperature to regional and ore-proximal alteration assemblages, distal to the intrusives. For this chapter, mineral assemblages for regional scale alteration were determined from paragenetic observations at a number of key localities within the Cloncurry District and broader Eastern Succession (Fig. 6.1). The spatial distribution of these assemblages is presented in the form of alteration maps. Mineral chemistry and stable isotope data from these assemblages

are compared with published and newly collected analyses from igneous and igneous-hosted metasomatic assemblages, and ore-proximal metasomatism. Data includes $\delta^{18}O$ analyses from mineral separates of magnetite, hematite, quartz, albite, K-feldspar and actinolite, major element chemistry of feldspar, pyroxene, amphibole and biotite, and trace element analyses of magnetite and hematite. Isotopic data and silicate mineral major element compositions have been acquired during this study, and compiled from a number of previous studies, while all oxide trace element chemistry presented was gathered during this study. A summary of data sources is given in Table 6.1.

6.1.1 Regional geology

The Eastern Succession of the Mt Isa Inlier can be divided into two main structural belts, namely the Mary Kathleen Fold Belt (MKFB) and Cloncurry District (Fig. 6.1). Supracrustal rocks in the Eastern Succession have been assigned by Blake (1987) into Cover Sequences 1, 2 and 3 deposited during distinct rift events at ca. 1870-1840 Ma, 1790-1720 Ma and 1680-1620 Ma respectively. Calc-silicate rocks, marbles, meta-siltstones, and mafic and felsic meta-volcanic rocks of the Mary Kathleen Group (Cover Sequence 2), including the Corella Formation, dominate the Mary Kathleen Fold Belt and much of the Cloncurry District. This sequence contains abundant metamorphic scapolite and is likely the metamorphosed equivalent of evaporitic marine carbonates (Ramsay & Davidson, 1970; Oliver et al., 1992). In the MKFB, and to a lesser degree in the Cloncurry District, Mary Kathleen Group stratigraphy was intruded by the Wonga and Burstall granite suites and associated mafic and felsic intrusives at ca. 1760 to 1720 Ma. Widespread sodic alteration accompanied intrusion, and Oliver et al. (1994) invoked dissolution of evaporitic sequences as a source of metasomatic salt.

Cover Sequence 3 stratigraphy, including the Soldiers Cap group, was emplaced over Cover Sequence 2, possibly by thrusting, in an early structural event (D_1). Upright, north-trending folds and pervasive fabric development are most commonly attributed to D_2 (e.g. O'Dea et al., 1997), and formed broadly synchronous with upper greenschist to amphibolite facies peak metamorphism at ca.

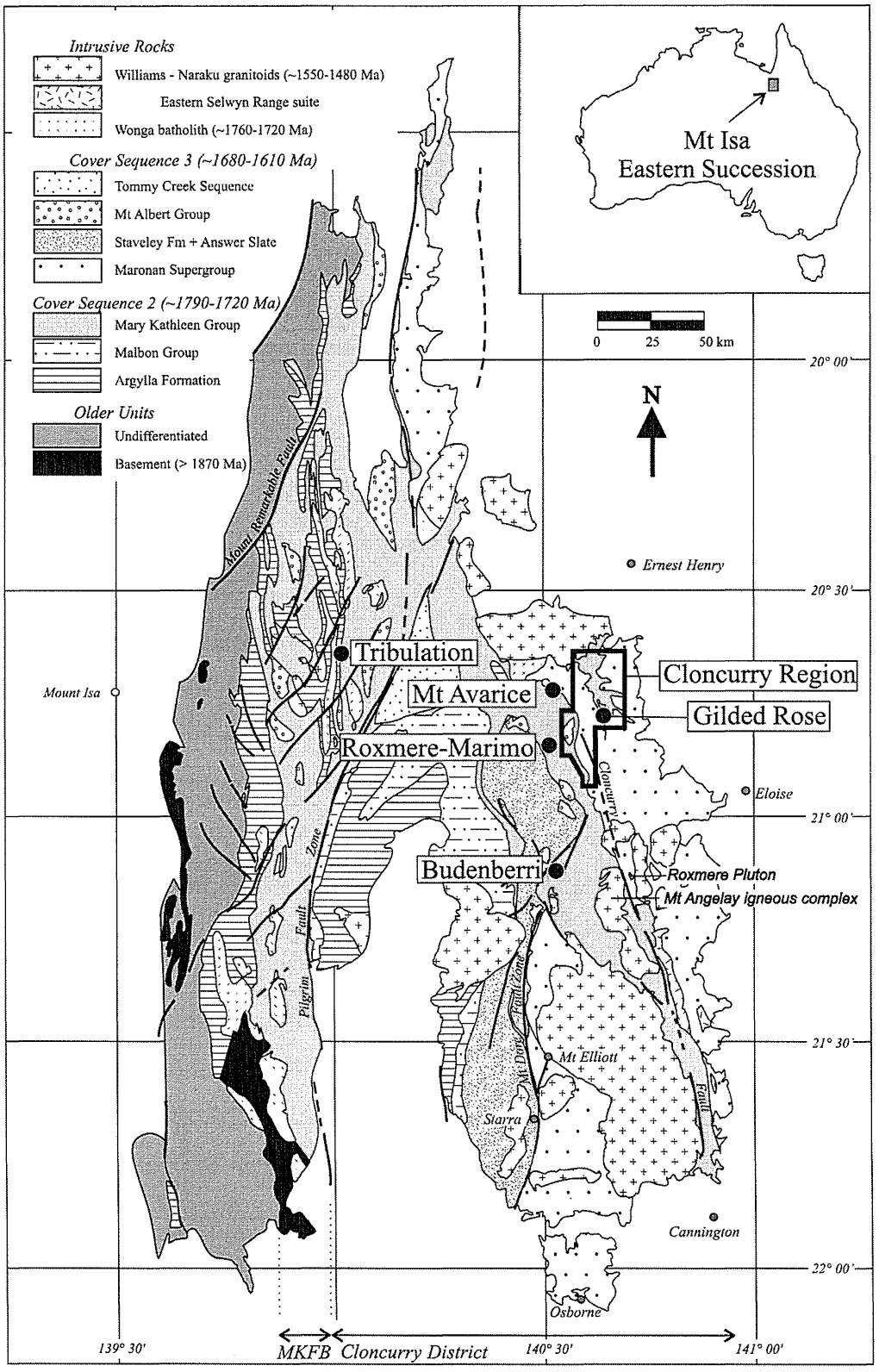

FIGURE 6.1.
Simplified geology of the Eastern Succession, modified after Williams (1998).

1600-1575 Ma (Page and Sun, 1998; Giles and Nutman, 2002; Hand and Rubatto, 2002). Emplacement of the Williams and Naraku batholiths (ca. 1550-1500 Ma) overlapped in time with retrograde deformation (D_3), and with extensive metasomatic fluid flow that is the focus of this contribution.

Metasomatic fluid sources and flow pathways

Within the Mt Angelay igneous complex and the adjacent Roxmere pluton (Fig. 6.1), previous researchers have documented ptygmatic aplite and pegmatite intimately associated with albite, actinolite and apatite ± magnetite and titanite assemblages (Tolman, 1998; Mark and Foster, 2000). Textures within these rocks are similar to unidirectional solidification textures documented in the roof zones of some porphyry stocks. As well, Perring et al. (2000) documented miarolitic and spherulitic, albite-, magnetite- and quartz-rich (± diopside, K-feldspar, biotite, titanite and pyrite) sills from the Lightning Creek prospect (Fig. 6.1). Complexly textured rocks at both Mt Angelay and Lighting Creek have been interpreted to record release of a fluid phase during crystallization, and these and similar intrusive bodies have been invoked as likely sources for fluids responsible for regional Na-(Ca) alteration (Mark and Foster, 2000; Perring et al., 2000).

The distribution of regional alteration assemblages records a variety of different structural conduits for metasomatic fluid flow. In the MKFB, fluid flow was predominantly focussed through breccias and fractures localized within brittle-ductile shear zones, and along contacts between units of markedly different competence (Oliver and Wall, 1987; Oliver et al., 1990). Large-aperture calcite veins (>1m width), hydrothermal breccias and associated Na-(Ca) alteration characterize the cores of these metasomatic systems. In the Cloncurry District, fluid flow was apparently more widespread, with extensive brecciation controlled in part by buckle folding of Corella Formation stratigraphy (**Chapter 4**, this study). Widespread breccias in the Mary Kathleen Group are referred to as Corella Breccias where minor clast transport is evident, and as Gilded Rose breccias (Cloncurry District) and Mt Philp breccias (MKFB) where significant clast transport is evident.

Numerous examples of Fe-oxide-related Cu±Au mineralisation exist throughout the Cloncurry District, and to a lesser extent the MKFB, and include such deposits as Ernest Henry, Osborne, Starra and Mt Elliott (Fig. 6.1). With the exception of Osborne, the majority of these deposits formed post-peak metamorphism, and existing geochronology suggests that in most cases mineralisation formed broadly synchronous with emplacement of the Williams and Naraku batholiths (Oliver et al., in revision). Despite similarities in relative timing, the deposits exhibit significant variations is mineralogy. For example, Mt Elliott, which lies adjacent to the Squirrel Hills pluton, exhibits a skarn-like albite, diopside, scapolite, actinolite, calcite, magnetite and sulphide rich mineral assemblage (Little, 1997). In contrast, Ernest Henry is distal to any know synchronous intrusives, and is characterized by a K-feldspar, biotite, amphibole, magnetite, calcite and sulphide rich mineral assemblage (Mark and Crookes, 1999).

6.2 METASOMATIC ASSEMBLAGES

Descriptions of metasomatic mineral assemblages from five key study areas are given below. Photographs of representative textures and mineral assemblages are presented in Figures 6.2 and 6.3 and corresponding paragenetic diagrams can be found in Figure 6.4.

6.2.1 Roxmere – Marimo area

Outcrops surrounding the Roxmere waterhole and the Marimo quarry occur within a brittle-ductile shear zone within Corella Formation stratigraphy of the northern Cloncurry District (Fig. 6.1). Details of the structural geology of the area have been described in **Chapter 5**. The area is characterized by an approximately 1km wide, NNW-trending zone of interconnected actinolite-rich shear-veins and breccias. These breccias and veins contain subordinate calcite, magnetite and quartz as infill. Breccia matrix, clasts and adjacent wallrock are intensely altered to albite ± actinolite, diopside, biotite, magnetite and titanite assemblages. Calcite-dominated extensional and extensional-shear veins, including the Marimo vein, cut the actinolite-rich breccias and veins. These extensional veins reach up to 5m in width,

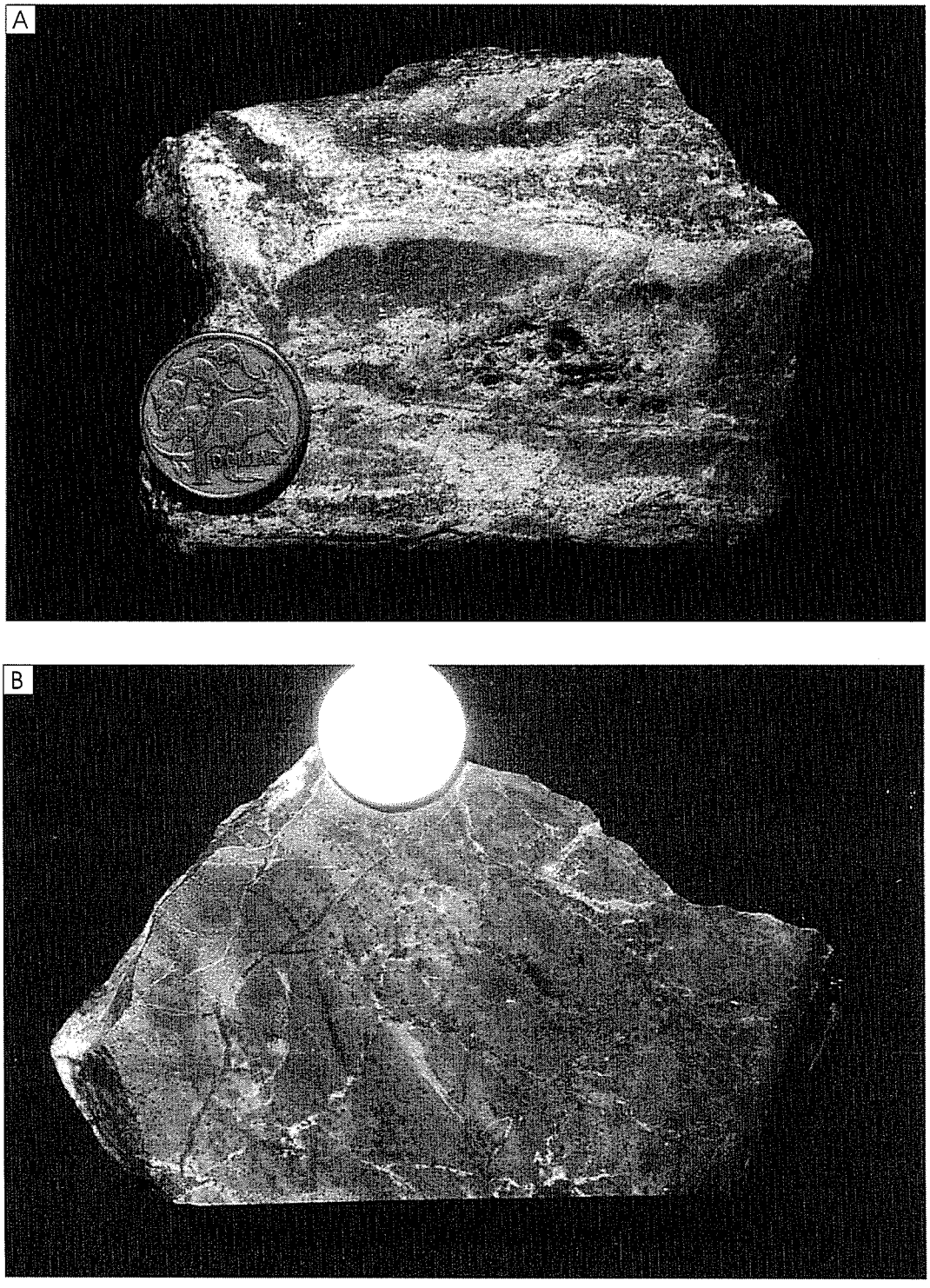

FIGURE 6.2.
Photographs of hand specimens of metasomatic rocks. Coin in each photo has a 2.4cm diameter. (a) Metasiltstone from an outcrop at the Roxmere waterhole, with distinct albitisation front (white). (b) Metasiltstone from the Budenberri rockhole, with well-developed actinolite crackle veins, and associated albitisation.
Continued on following page.

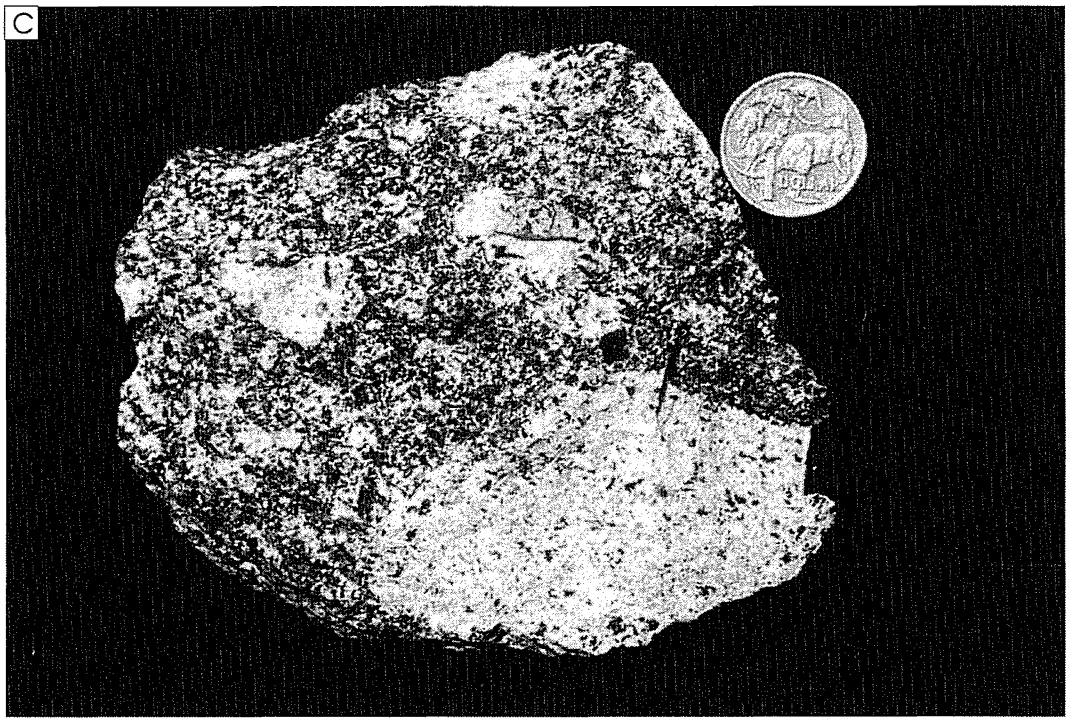

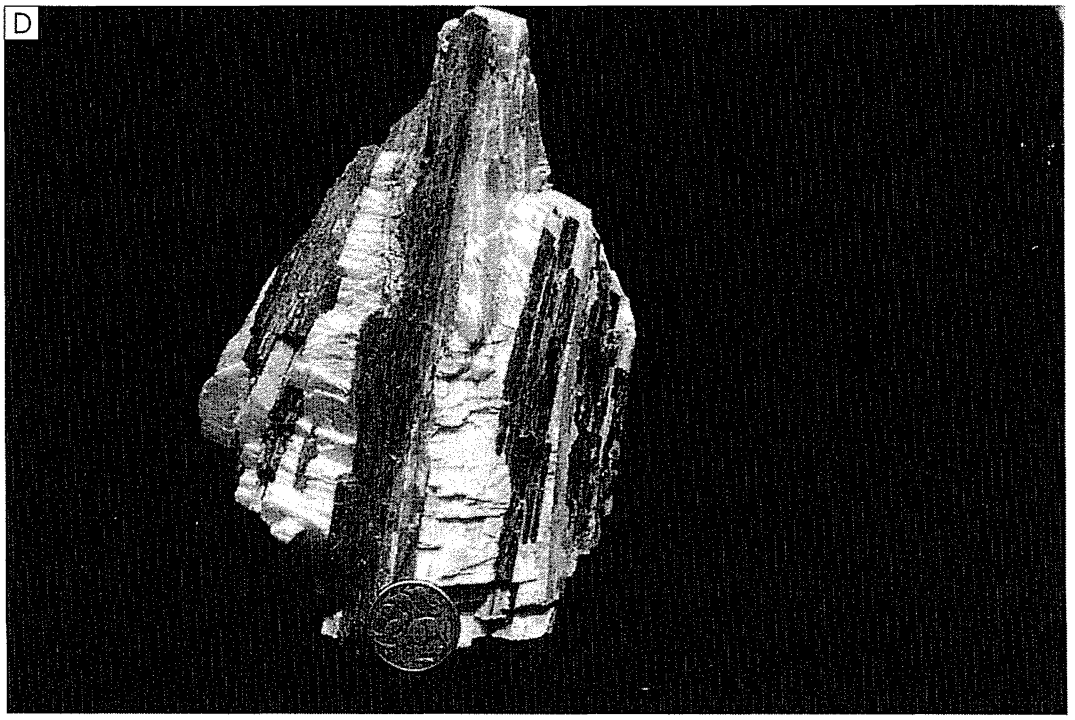

FIGURE 6.2. (continued)
Photographs of hand specimens of metasomatic rocks. Coin in each photo has a 2.4cm diameter. (c) Milled breccia from the Tribulation quarry, with intensely albite -altered clasts (white) and albite and actinolite altered matrix (white and grey). (d) Coarse-grained calcite and actinolite infill from the Tribulation vein.
Continued on following page.

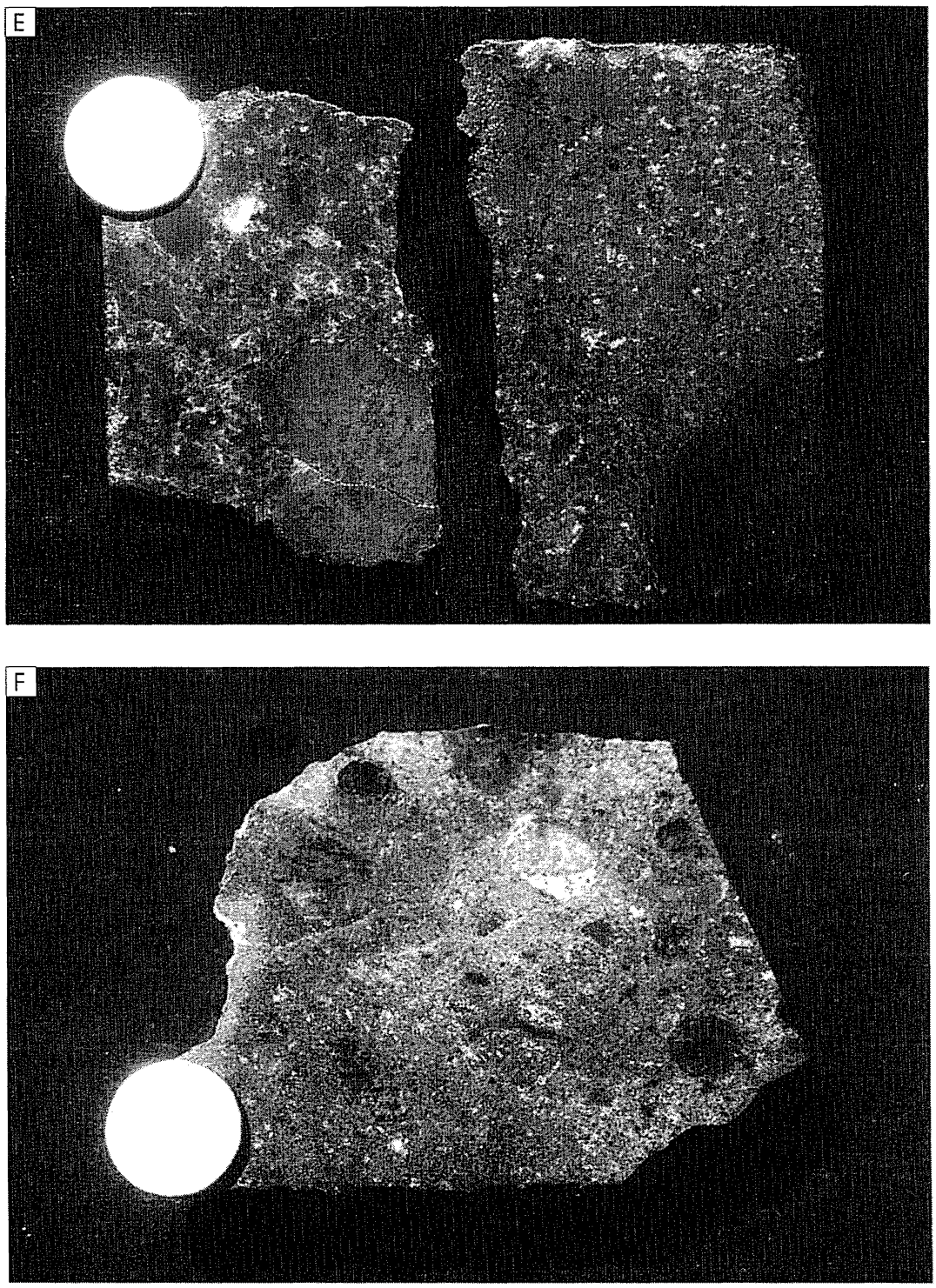

FIGURE 6.2. (continued)
Photographs of hand specimens of metasomatic rocks. Coin in each photo has a 2.4cm diameter. (e) Milled, infill-rich breccias with intense "redrock" hematite-dusting of matrix feldspars. Samples are from the Gilded Rose type area (left) and Camel Hill (right). (f) Polymict, milled chlorite-rich breccia from the Mt Avarice Quarry. Note clasts of early-formed quartz vein (white) and dolerite (dark grey).

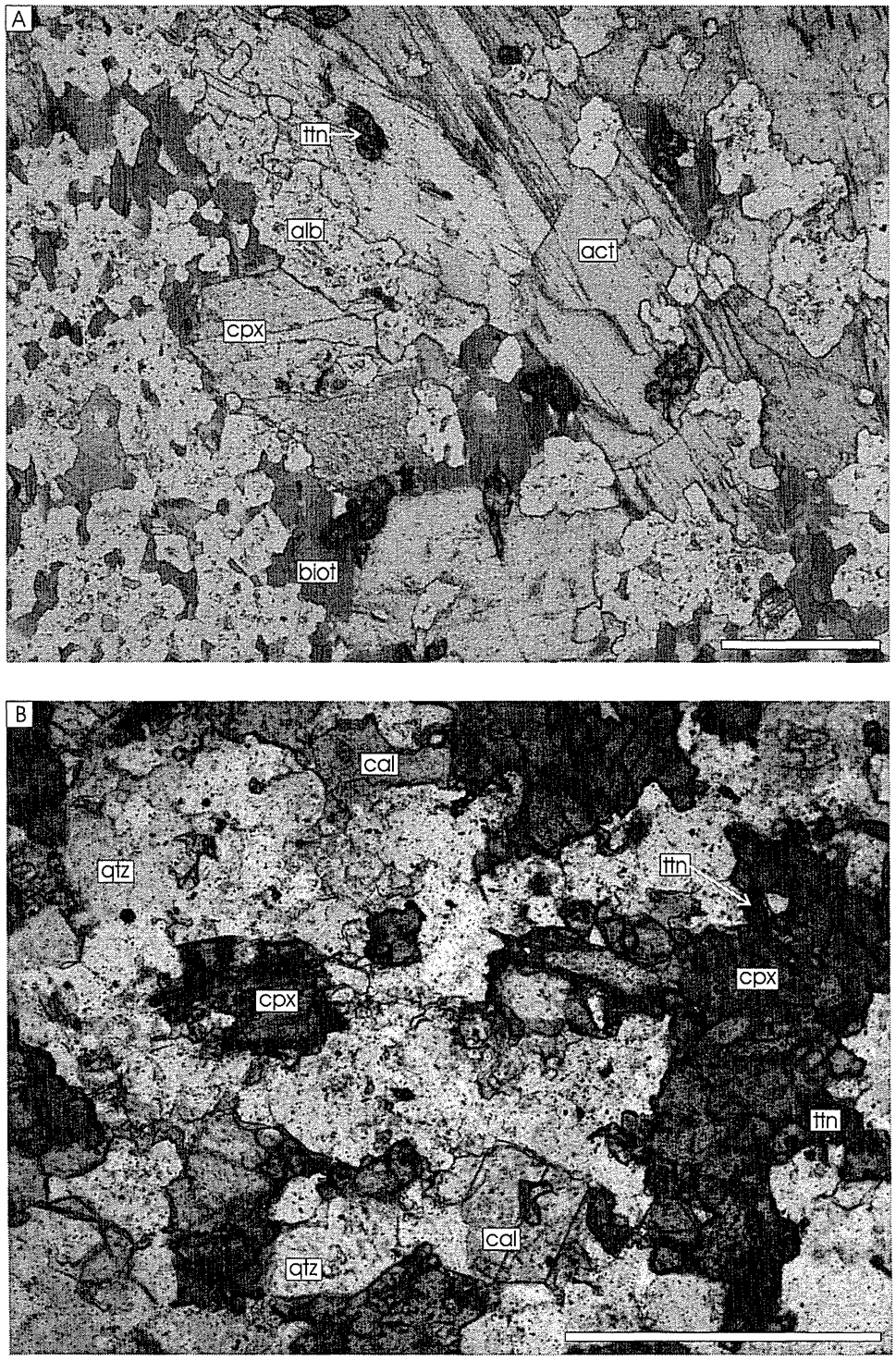

FIGURE 6.3.
Photomicrographs of typical metasomatic assemblages. Scale bar in each photo is 500 microns. All photos in plane polarized light, except where noted. (a) Albite, actinolite, diopside, biotite and titanite rich breccia from the Roxmere-Marimo area. (b) Early, diopside-rich contact metasomatic (skarn) assemblages at the Budenberri Rockhole. Continued on following page.

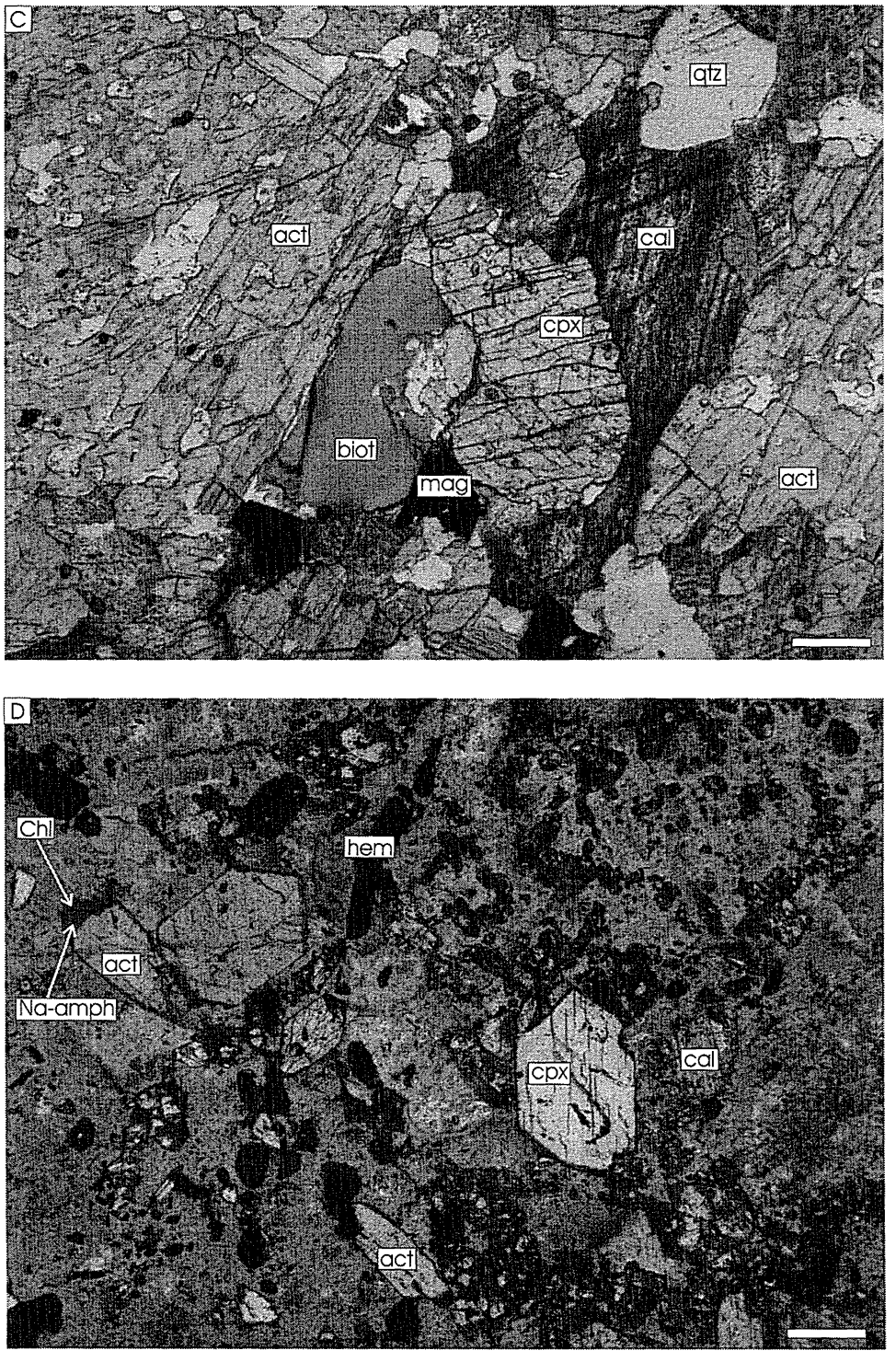

FIGURE 6.3. (continued)
(c) Coarse-grained calcite, actinolite, biotite diopside, quartz and magnetite infill from the Tribulation vein. (d) Grungy, hematite-dusted matrix, typical of Gilded Rose breccias. Note euhedral hematite, and successive sodic-amphibole and chlorite overgrowths on actinolite. Continued on following page.

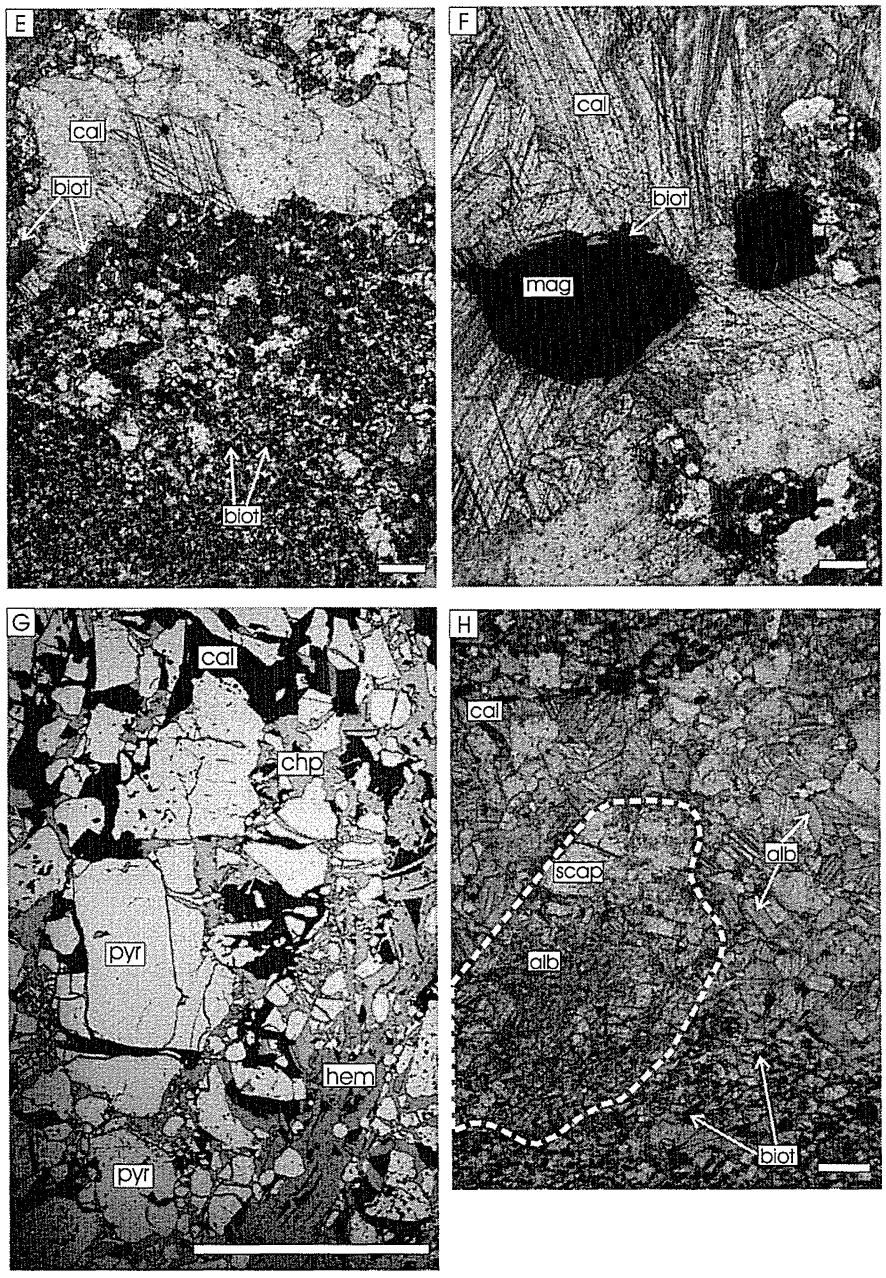

FIGURE 6.3. (continued)
(e - f) Crackle veins from the Mt Avarice quarry cutting calc-silicate rocks. The coarse grain-size of alteration and infill biotite readily distinguishes metasomatic biotite from metamorphic biotite. (g) Dolerite-hosted multistage vein from the Mt Avarice quarry, with early pyrite (+ quartz, actinolite and magnetite, not shown) cut and overgrown by calcite, chalcopyrite and hematite. Photomicrograph is in reflected light. (h) Weakly albitised calc-silicate rock with metamorphic biotite, calcite, K-feldspar and scapolite assemblage. Note replacement of large scapolite grain (outlined) by fine-grained albite.

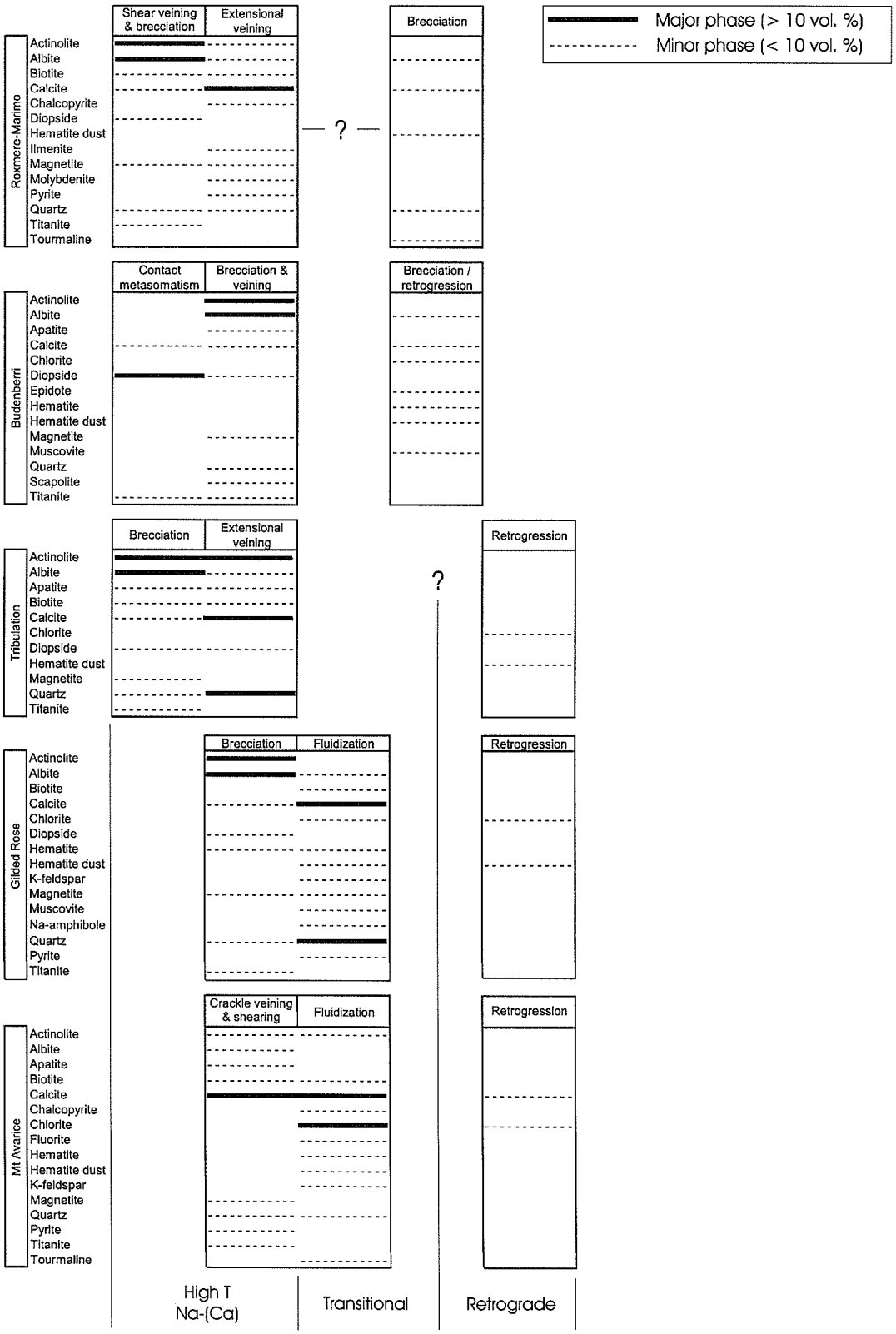

FIGURE 6.4.
Paragenetic diagrams for key field areas referred to in the text.

and contain subordinate actinolite, quartz, biotite, magnetite, ilmenite, chalcopyrite, pyrite and molybdenite, and are associated with broad zones of albitisation. Calcite veins are largely recrystallised to <1cm grains, but locally preserve grains >5cm. Similar large aperture calcite veins have been described by Oliver et al. (1993) in the Mary Kathleen Fold Belt, and are interpreted as occurring within the fluid-buffered cores of large metasomatic flow systems.

Several magnetite-rich metasomatic ironstones are also present in the area, and contain subordinate calcite, quartz, actinolite and minor pyrite. These are typically deformed with magnetite- and/or quartz-rich portions being fractured, boudinaged and enveloped by less competent calcite. Locally magnetite is pseudomorphed by hematite. Spatially restricted breccias with pink hematite stained albite and black tourmaline alteration are also present in the area. These contain vuggy, epithermal-like quartz ± calcite infill. Their relation to more widespread albite- and actinolite-rich assemblages is unconstrained.

6.2.2 Budenberri

The Budenberri rockhole lies on the NW-dipping limb of an open fold developed in marble, calc-silicate rock and meta-siltstone stratigraphy of the Doherty Formation (Corella Formation equivalent) in the central Cloncurry District (Fig. 6.1). Brecciation in the Budenberri area was localized by D_3 folding, with which it is likely synchronous (**Chapter 4**, this study). At the Budenberri rockhole, calc-silicate rocks and meta-siltstones exhibit pervasive fine-grained diopsidic clinopyroxene and subordinate titanite alteration. While the distribution of clinopyroxene could not be directly related to specific metasomatic fluid conduits (i.e. fractures or breccias), similar stratigraphy in the broader Budenberri region does not contain abundant clinopyroxene away from areas of brecciation and veining. Consequently, early clinopyroxene is interpreted as a contact metamorphic/metasomatic product. Granitoids crop out within 4 km of the rockhole, and are inferred to underlie the area.

Albite and actinolite ± diopside, scapolite, calcite, quartz, titanite, magnetite and apatite rich breccias and veins cut early diopside-rich assemblages. These vary

from sheeted albite and scapolite veins with actinolite- and titanite-rich selvages, to broad zones of albite, actinolite, clinopyroxene and titanite alteration associated with crackle through to mosaic and milled breccias. Locally, milled breccias are characterised by intense hematite staining and retrogression of feldspars (to muscovite), and diopside and actinolite (to chlorite). These assemblages are in turn cut by microfractures with euhedral epidote and albite grains, suggesting multiple late metasomatic and structural episodes at conditions that were retrograde relative to early diopside-actinolite alteration.

6.2.3 Tribulation calcite vein

The Tribulation – Lime Creek (TLC) fault cuts meta-siltstone, calc-silicate rocks, marble, and meta-dolerite of the lower Corella Formation in the Mary Kathleen Fold Belt (Fig. 6.1). Within the fault zone, bodies of cataclastic and magmatic-hydrothermal breccias are common. These breccias are matrix supported, and contain rounded clasts derived from the immediate wallrocks. Breccia matrix and clasts are intensely altered to actinolite, albite ± calcite, quartz, apatite, diopside, biotite, and titanite assemblages. The large aperture Tribulation vein cuts the breccias, and is one of several hundred similar veins throughout the Mary Kathleen Fold Belt (Oliver et al., 1993). The Tribulation vein is extremely coarse-grained and exhibits a well-defined mineral zonation. Apatite, titanite, biotite, quartz and diopside grains approaching 20cm across as well as rare small magnetite grains (<5mm) are found immediately adjacent to the vein margins, actinolite crystals over 1m in length radiate inwards from these, and coarse calcite crystals in excess of $1m^3$ dominate the core of the vein. Minor retrogression of the above mineralogy is evident, most notably recrystallization and hematite dusting of albite, and chloritisation of actinolite and clinopyroxene.

6.2.4 Gilded Rose breccia type area

At the Gilded Rose breccia type area a pipe-like breccia body has intruded schists and amphibolites of the Soldiers Cap Group. Breccia clasts are dominated by Corella Formation lithologies, and appear to have been transported upwards in the

breccia (**Chapter 5**). The breccia body can be divided into an irregular NW-trending splay, and an elliptical, N-trending main zone. Both zones contain early milled magmatic-hydrothermal breccias with a low component of infill, and pervasive albite, actinolite ± calcite, diopside, magnetite, quartz and titanite alteration. In the main breccia zone, these breccias and alteration assemblages are transitional to, and overprinted by infill-rich polymictic breccias with calcite ± biotite, chlorite, hematite, K-feldspar, pyrite, muscovite, and Na- to Na-Ca amphibole assemblages. Na- to Na-Ca amphiboles form euhedral overgrowths on actinolite grains, while hematite occurs as replacement of magnetite, overgrowths on magnetite grains, and as isolated euhedral laths. The remaining chlorite, biotite, calcite, K-feldspar and muscovite also form the infill and matrix to the main zone breccias, commonly as euhedral mineral grains. Calcite grains preserve growth zoning evident in cathodoluminescence imagery (**Chapter 7**) that is consistent with calcite precipitation in vugs within the main phase breccias. These textural characteristics suggest that the inferred lower temperature chlorite-bearing mineral assemblages accompanied or immediately followed the high-infill component brecciation event, inferred in **Chapter 5** to mark upward transport of breccia clasts by magmatic-hydrothermal explosion and/or gas streaming. Limited retrogression of the above mineral assemblages in the form of chloritic microfractures and minor accompanying hematite dusting of feldspars is locally evident.

6.2.5 Mt Avarice quarry

A multi-stage metasomatic event hosted by scapolitic calc-silicate rocks, marbles, meta-siltstones and dolerite is well exposed in the Mt Avarice quarry on the outskirts of Cloncurry. Widespread brittle-ductile deformation is marked by intense shearing of marbles, crackle-brecciation of meta-siltstones, and localised veining of dolerite. Intense shearing may have facilitated weak albite and actinolite alteration of marble. Crackle breccias in the meta-siltstones are characterized by quartz and calcite ± actinolite, magnetite, biotite and apatite infill with albite, actinolite and biotite alteration, including the replacement of metamorphic scapolite by albite. Despite similar mineral assemblages, the Mt Avarice veins are smaller,

and alteration is less intense than in other areas such as Roxmere-Marimo and Tribulation, and may indicate a distal position within similar alteration systems, and/or a smaller net fluid flux. Where these veins cut dolerite, quartz, calcite, actinolite and magnetite are precipitated synchronously with pyrite. The lack of significant pyrite associated with similar assemblages outside of the dolerite may indicate a local sulphur source. Crackle breccias, sheared marbles and veined dolerite are all cut by milled breccias with calcite and chlorite ± quartz, K-feldspar, actinolite, biotite, hematite, tourmaline and fluorite metasomatic assemblages. These breccias vary from green to red reflecting varying concentrations of chlorite and hematite-stained feldspar. Early veins in the dolerite are in places re-fractured with calcite, hematite and chalcopyrite cutting and overgrowing quartz, actinolite, magnetite and pyrite assemblages. Chalcopyrite occurs only where earlier pyrite is present. Minor retrogression is noted in all rock types, and is characterized by chlorite and calcite micro-fracturing.

6.2.6 Correlation of metasomatic assemblages

Based on the above observations, three broad metasomatic classes are distinguished (Fig. 6.4). The first of these is characterized by high temperature albite and actinolite ± quartz, calcite, magnetite, diopside, scapolite, apatite, biotite and titanite, and locally pyrite, chalcopyrite, molybdenite and ilmenite assemblages. Combined these are referred to here as "Na-(Ca)" assemblages. Within this broad class there are clearly variations in structural style and specific mineral assemblages, with for example, diopside-rich contact metasomatism, albite- and actinolite-rich shear veining and brecciation and large aperture calcite veining all evident. Further, there is no direct indication that Na-(Ca) metasomatic assemblages were synchronous throughout the Eastern Succession, and may reflect multiple metasomatic pulses, that were either temporally overlapping or distinct.

A second broad metasomatic class is recognized, and is best developed at the Gilded Rose type area and the Mt Avarice Quarry. This is characterized by metasomatic assemblages that include calcite, quartz and chlorite ± K-feldspar (and/or subordinate albite), actinolite (and/or Na- to Na-Ca-amphibole), biotite,

hematite (and/or subordinate magnetite), epidote, muscovite, fluorite, tourmaline, pyrite and chalcopyrite. These assemblages commonly contain euhedral grains within veins, and as matrix and infill minerals in milled and transported polymictic breccias. These are termed "Transitional" assemblages, as they contain intermediate assemblages between high temperature Na-(Ca) metasomatism, and a third "Retrograde" chlorite- and calcite-bearing metasomatic class that lacks amphibole. Both Transitional and Retrograde metasomatic assemblages are commonly accompanied by intense red-rock staining of feldspars by hematite dusting.

6.2.7 Spatial distribution of metasomatic assemblages

Metasomatic rocks are extremely widespread in the Eastern Succession, particularly within the Corella and equivalent formations. Figure 6.5 illustrates the distribution of Na-(Ca) and Transitional to Retrograde (red-rock) metasomatic assemblages in the Cloncurry Region, an area of complexly folded and metasomatised rocks to the east of Cloncurry. These alteration distribution maps have been constructed from field observations at greater than one thousand outcrops, and classification of greater than five hundred hand specimens. Alteration mapping was focussed within Corella Formation stratigraphy (Cover Sequence 2), and should be considered approximate within Cover Sequence 3.

In Figure 6.5, a general correspondence is seen between the distribution of post-peak metamorphic intrusive units and Na-(Ca) alteration. This is particularly noted in the inferred roof zone of the Outer Naraku pluton (see **Chapter 2**, this study), in the extreme NW corner of the map area. Transitional and Retrograde alteration assemblages are also widespread, and their distribution shows a general correspondence with late NNE- to NNW-trending fault zones. This is particularly evident along segments of the Cloncurry fault zone, and at the Gilded Rose breccia type area.

6.3 ISOTOPE GEOCHEMISTRY

Isotopic analyses of $\delta^{18}O$ ratios of metasomatic silicate and oxide minerals were undertaken in order to estimate fluid isotopic signatures, and temperatures of

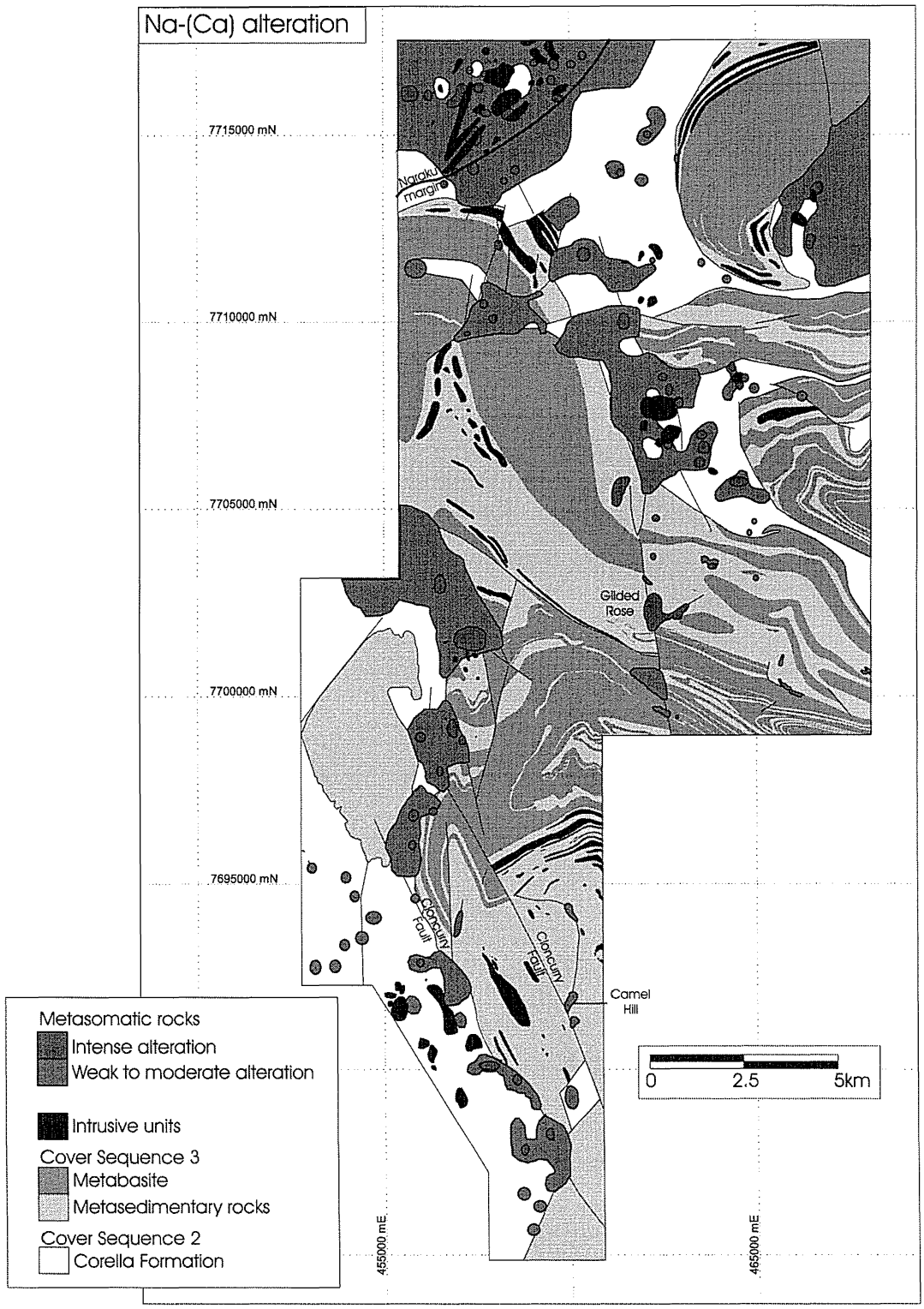

FIGURE 6.5.
Alteration distribution maps for the Cloncurry Region, east of the town of Cloncurry (Fig. 6.1). Maps are constructed from field observations and hand specimen classification.

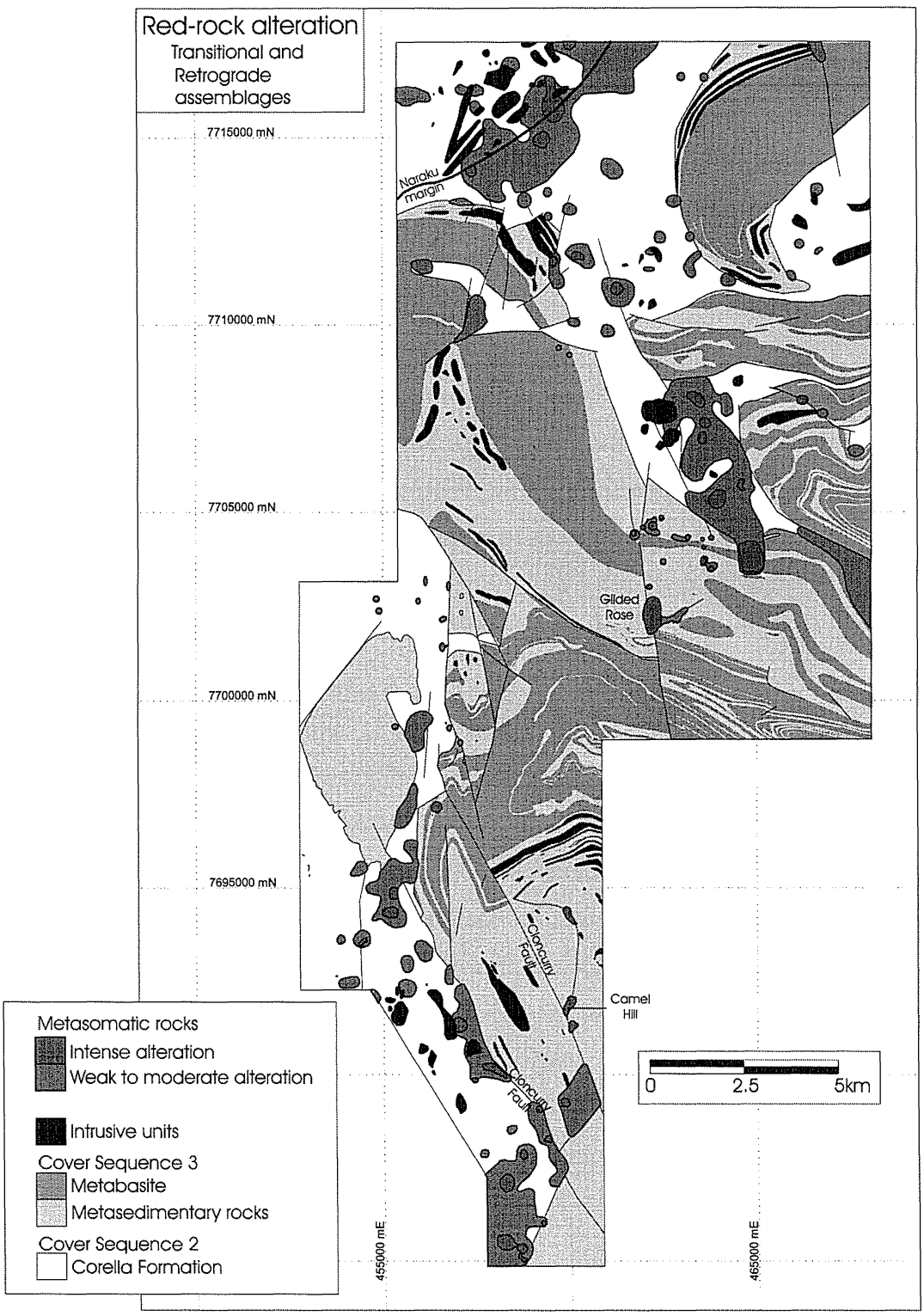

FIGURE 6.5. (continued)
Alteration distribution maps for the Cloncurry Region, east of the town of Cloncurry (Fig. 6.1). Maps are constructed from field observations and hand specimen classification.

mineral precipitation. For this study, 34 samples of magnetite, hematite, quartz, albite and actinolite were obtained by sample crushing, sieving, magnetic separation and hand-picking. All samples were cleaned in a sonic bath prior to analysis of 1 to 2 mg using the laser fluorination technique of Sharp (1989), with isotopic analysis on a Finnigan Delta^{Plus} XL mass spectrometer at the University of New Mexico (UNM). $\delta^{18}O$ values are reported relative to V-SMOW (Table 6.2). Duplicates of seven accompanying samples were also analysed by standard techniques at the U.S. Geologic Survey (USGS) stable isotope lab, Colorado, involving extraction of oxygen gas by reaction with BrF_5, and subsequent conversion to CO_2 for analysis (Clayton and Mayeda, 1963). Duplicate analyses from the USGS were on average 0.23‰ higher than analyses from UNM, with a maximum variation of 0.8‰. Further analyses compiled from a variety of settings throughout the Eastern Succession are also presented (Table 6.1), and were analysed using standard fluorination techniques (Clayton and Mayeda, 1963).

6.3.1 $\delta^{18}O$ vs. $\delta^{18}O$ plots

A number of $\delta^{18}O$ vs. $\delta^{18}O$ plots are presented in Figure 6.6 for equilibrium metasomatic mineral pairs from regional alteration assemblages. All data presented in Figure 6.6 was collected for this study. Given the variation in fractionation factors with temperature for different minerals, such plots can yield information as to both the temperature of mineral precipitation, and the $\delta^{18}O$ signature of the metasomatic fluid. In each plot, a grid has been constructed from equilibrium curves at constant temperature (straight lines) and constant fluid $\delta^{18}O$ signature (curved lines), using fractionation factors of Zheng (1991 and 1993). For quartz-magnetite mineral pairs, a grid has also been constructed using fractionation factors of Bottinga and Javoy (1973), although this grid is only valid for temperatures of 500°-800°C.

Figures 6.6a, b and c are $\delta^{18}O$ vs. $\delta^{18}O$ plots for quartz-magnetite, actinolite-magnetite and quartz-actinolite mineral pairs representative of regional Na-(Ca) to Transitional mineral assemblages. Of these pairs, quartz-magnetite is considered the best for temperature estimates due to the large $\delta^{18}O$ fractionation between these

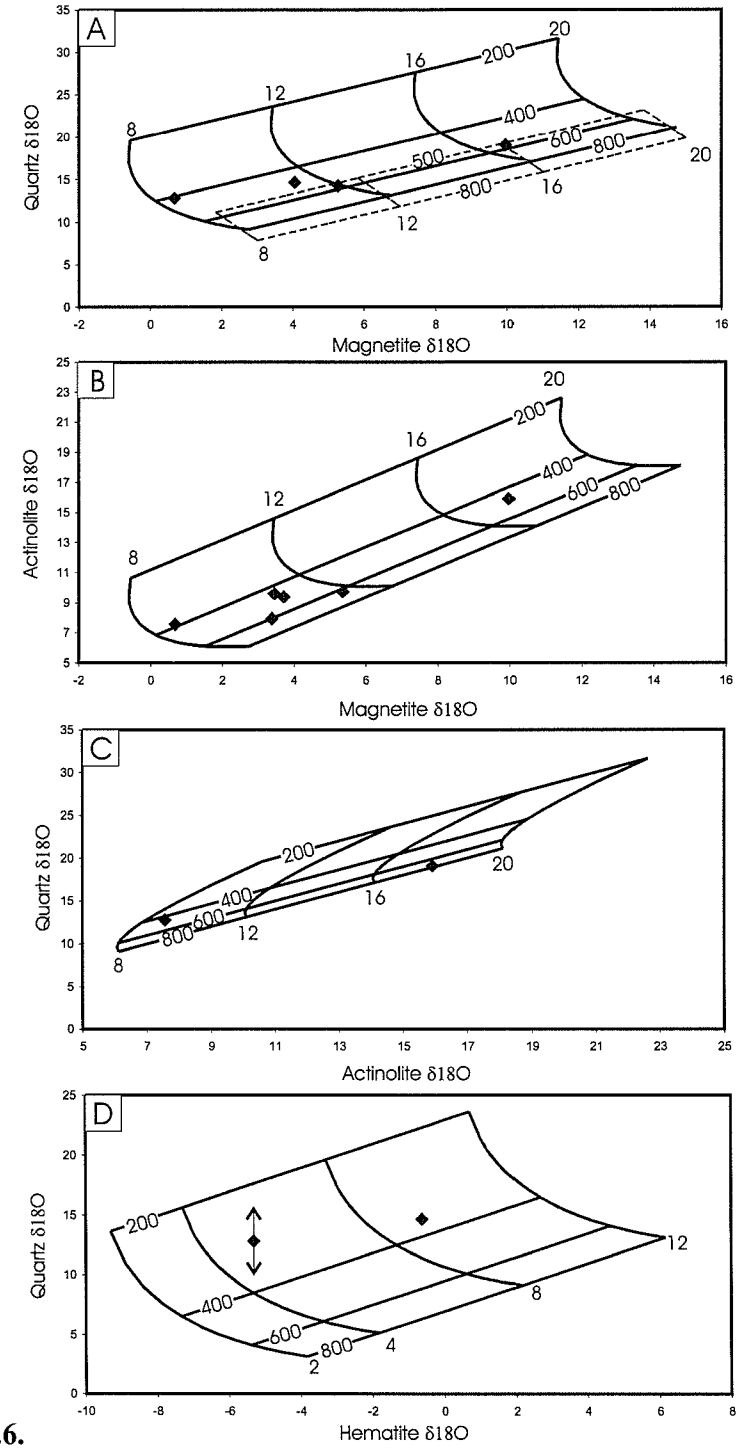

FIGURE 6.6.
$\delta^{18}O$ vs. $\delta^{18}O$ plots for metasomatic mineral pairs. Temperature-composition grids are constructed from fractionation factors of Zheng (1991 and 1993; solid lines) and Botinga and Javoy (1973; dashed lines). (a-c) Mineral pairs representative of Na-(Ca) alteration assemblages indicate temperatures predominantly between 400° and 600°C. (d) Hematite-quartz mineral pairs representative of Transitional mineral assemblages indicate cooler temperatures (likely <400°C). For the low $\delta^{18}O^{hematite}$ sample, hematite, chalcopyrite and calcite cut and overgrow quartz, magnetite, actinolite and pyrite, indicating possible isotopic disequilibrium between hematite and quartz. Regardless, the low $\delta^{18}O^{hematite}$ value requires low $\delta^{18}O^{fluid}$ composition (likely < 6‰).

minerals (Fig. 6.7). All quartz-magnetite pairs yield temperature estimates between 400° and 600°C. Similar estimates are achieved for actinolite-magnetite and quartz-actinolite pairs, but with greater spread in the data, likely reflecting poor resolution of these pairs as geothermometers. Fluid $\delta^{18}O$ estimates cluster between 8 and 12‰, with some outliers at higher $\delta^{18}O$ values. At high temperatures (ca. 500°C) quartz-magnetite pairs record significant variations in $\delta_{18}O^{fluid}$ values with negligible temperature variation, while coupled shifts in temperature and $\delta_{18}O$ fluid are noted at lower temperatures. One possibility is that these trends may indicate isotopic signatures being controlled by equilibration with isotopically heavy wallrocks at high temperatures and by input of isotopically light fluid at low temperature.

Two quartz-hematite mineral pairs were analysed from Transitional to Retrograde breccias and veins (Fig. 6.6d). For one of these, quartz and hematite are in textural equilibrium, while the other is a multistage vein, with early quartz, magnetite, actinolite and pyrite being cut and overgrown by calcite, hematite and chalcopyrite (Fig. 6.3g). The very low $\delta^{18}O^{hematite}$ value for this sample (-5.3‰) necessitates a low $\delta^{18}O^{fluid}$ composition (< ~6‰). Both samples record temperature estimates below 400°C, although this may not be accurate in the multistage vein.

6.3.2 $\delta^{18}O$ histograms

In Figure 6.8, histograms of $\delta^{18}O$ values for magnetite, hematite, quartz, albite, K-feldspar and actinolite are presented, comparing isotopic ranges for regional and deposit-scale metasomatism, with ranges for igneous assemblages. The term igneous is used loosely in this section to include both magmatic and igneous-hosted metasomatic minerals, including inferred magmatic-hydrothermal interface minerals.

On average, magnetite, quartz and actinolite all show distinct shifts to higher $\delta^{18}O$ values in regional alteration assemblages relative to igneous minerals. This may reflect an increase in $\delta^{18}O^{fluid}$ in regional alteration relative to igneous assemblages. Alternatively it may represent a cooling trend for quartz and actinolite, and a heating trend for magnetite (Fig. 6.7), although this variance seems highly unlikely given the close association of quartz, actinolite and magnetite in regional

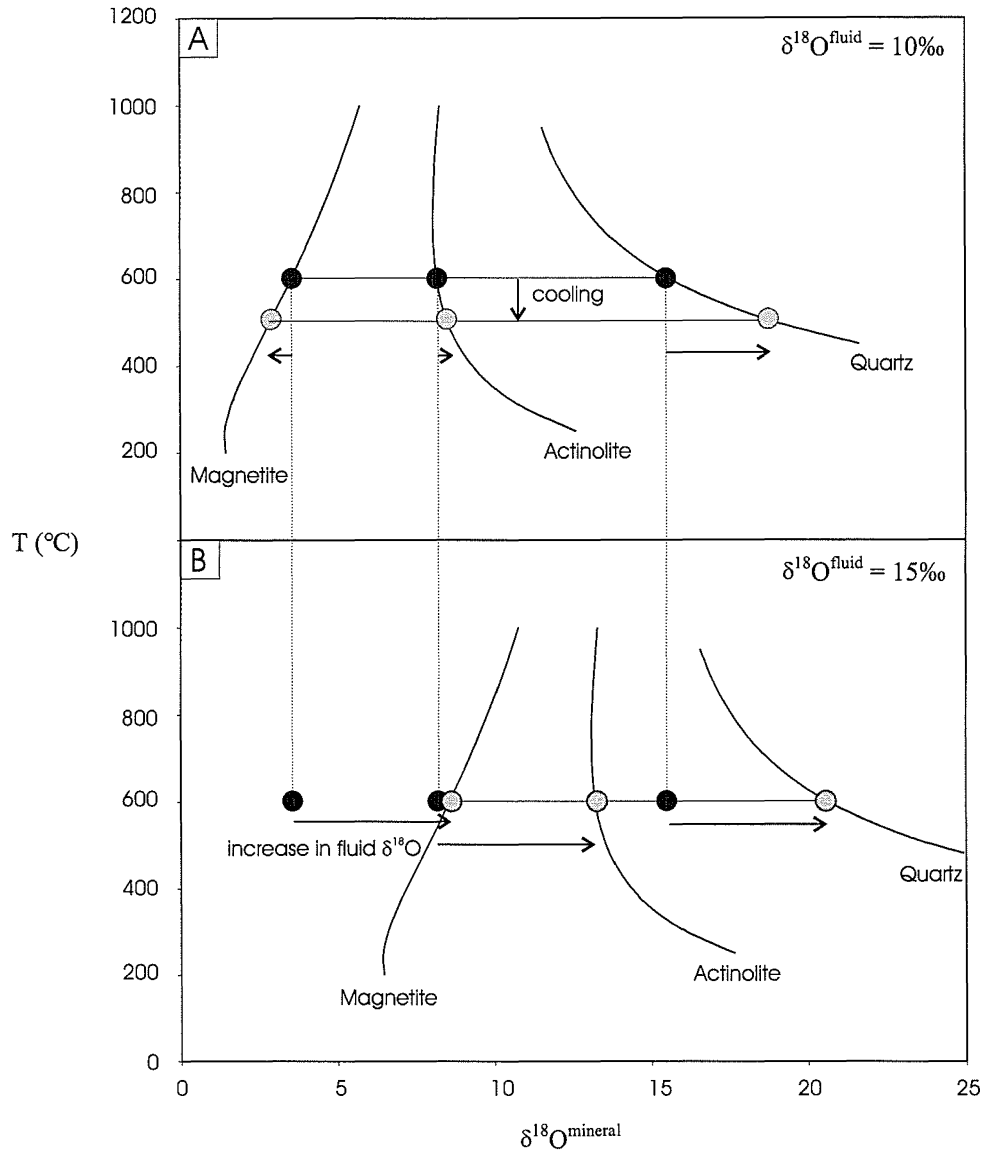

FIGURE 6.7.
Fractionation curves reflect the isotopic ratios of magnetite, actinolite and quartz in equilibrium with a fluid of given isotopic composition, as a function of temperature. Fractionation factors are from Zheng (1991 and 1993). Quartz-magnetite pairs are favored as geothermometers due to the large difference in fractionation factors. (a) An increase in $\delta^{18}O$ values of quartz and actinolite, with decreases in magnetite $\delta^{18}O$ can be explained by cooling. (b) Coupled increases in $\delta^{18}O$ values of magnetite, quartz and actinolite require input of isotopically heavier oxygen.

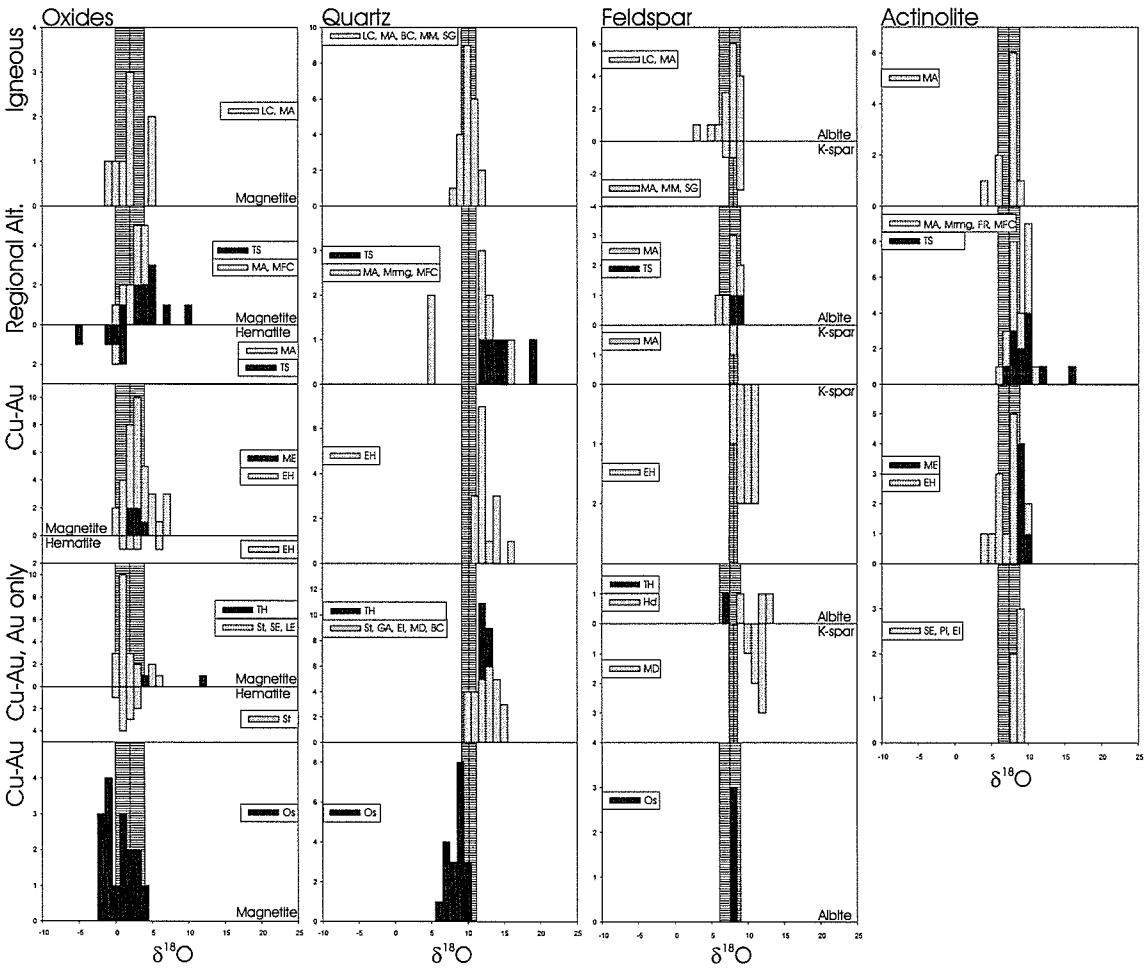

FIGURE 6.8.
Cumulative histograms for silicate and oxide minerals in igneous (including igneous hosted metasomatic) rocks, regional alteration, and Cu±Au ore-proximal metasomatism. Horizontal shading indicates mean isotopic values ± one standard deviation for igneous minerals. See text for discussion. LC = Lightning Creek, MA = Mt Angelay and Roxmere pluton, BC = Bull Creek, MM = Mt Margaret, SG = Saxby granite, MFC = Mt Fort Constantine, TS = this study, Mrmg = Marramungee, FR = Fullarton River, ME = Mt Elliott, EH = Ernest Henry, St = Starra, SE = Southern Extensions, LE = Little Eva, GA = Great Australia, El = Eloise, MD = Mt Dore, Hd = Houdini, Pl = Plume, TH = Tick Hill, Os = Osborne.

alteration assemblages. Two quartz samples from Mt Angelay do not follow this trend and record a distinct $\delta^{18}O$ depletion relative to igneous quartz. These samples are from paragenetically late epithermal veining described by Mark (1998a), and likely record a distinct, low $\delta^{18}O$ fluid. Albite exhibits a similar range in $\delta^{18}O$ values for both regional alteration and igneous assemblages. Hematite shows a demonstrable depletion in $\delta^{18}O$ relative to igneous-associated magnetite. Much of this difference can be attributed to the difference in fractionation factors for magnetite and hematite, with a ca. 2‰ lower $\delta^{18}O$ signature expected for hematite relative to magnetite at 300°C. However, a single hematite analysis at –5.3‰ collected for this study must indicate cooling and/or or input from an isotopically lighter oxygen source relative to the igneous samples.

Analyses from the Mt Elliott deposit record a narrow range in isotopic ratios, with similar magnetite signatures, and slightly ^{18}O-enriched actinolite signatures relative to igneous assemblages. This enrichment may record cooling or input of a small component of isotopically heavier oxygen. In contrast, Ernest Henry samples exhibit a wider range in $\delta^{18}O$ ratios. For magnetite and hematite, Ernest Henry samples overlap with, and extend to higher $\delta^{18}O$ ratios than recorded by the igneous minerals. This shift either records higher temperatures at Ernest Henry, or a component of isotopically heavier oxygen. This is particularly true for the hematite samples, as at a given temperature hematite should record slightly lower $\delta^{18}O$ values than for magnetite (ca. 2% lower at 300°C and ca. 1% lower at 500°C). Ernest Henry quartz and K-feldspar show overlapping but clearly increased $\delta^{18}O$ values relative to igneous minerals, while Ernest Henry actinolite and igneous-hosted actinolite have a similar range in $\delta^{18}O$.

Data is available from a number of other Cu±Au deposits and prospects, including Starra, Tick Hill, Southern Extensions, Little Eva, Great Australia, Eloise, Mount Dore, Bull Creek, Houdini and Plume. Analyses from these localities record similar to slightly enriched magnetite and actinolite $\delta^{18}O$ ratios relative to igneous values, and marked increases in quartz, albite and K-feldspar $\delta^{18}O$ ratios. This likely records both cooling and input of isotopically heavier oxygen. Hematite from Starra has similar $\delta^{18}O$ values to Ernest Henry hematite.

In contrast to the above deposits, Osborne samples record a marked decrease in $\delta^{18}O$ for both magnetite and quartz relative to igneous magnetite. This clearly indicates a different isotopic character to the Osborne deposit relative to other Cu±Au deposits in the Eastern Succession.

6.3.3 Summary

On the whole, metasomatic magnetite, quartz, albite, K-feldspar and actinolite overlap with and extend to higher $\delta^{18}O$ values than recorded for igneous assemblages. The clustering of data is consistent with metasomatic fluids being predominantly derived from or equilibrated with igneous rocks. While cooling may have resulted in a shift to higher $\delta^{18}O$ ratios in the silicate minerals, it could not have done so for magnetite, and as such, input of isotopically heavy oxygen was likely the dominant mechanism for increasing $\delta^{18}O$ signatures relative to igneous values. Metamorphic sequences of the Eastern Succession are the most probable source for ^{18}O-enriched oxygen. In particular, least-altered marbles and calc-silicate rocks of the Corella Formation have been shown to contain markedly heavier oxygen signatures than igneous rocks in the region (Oliver et al., 1993; **Chapter 7**, this study), and many samples, particularly those collected for this study, were hosted within Corella Formation stratigraphy. Only a few samples show marked decreases in $\delta^{18}O$ relative to igneous values. These include hematite and quartz from regional scale alteration, but with the exception of Osborne samples, do not include any significant analyses from deposit-scale alteration and mineralisation. The low $\delta^{18}O$ analyses from both regional alteration and Osborne record input of isotopically light oxygen and/or variations in temperatures relative to igneous assemblages.

6.4 SILICATE CHEMISTRY

In this section, mineral chemistry of amphibole, biotite, pyroxene and feldspar is investigated in order to characterize variations between metasomatic assemblages that may relate to variations in fluid chemistry. Chemical analyses were performed with a Jeol JXA-840 microprobe, using an energy-dispersive collector at James Cook University. 5 μm spots were analysed for 40 seconds at

filament conditions of 10nA and 15kV. ZAF matrix corrections were carried out using Moran Scientific software. Representative microprobe analyses are presented in Table 6.3. Data compiled from other sources was collected using the same instrument at James Cook University, and using similar analytical procedures.

In the hydrous minerals biotite and amphibole, significant substitution of Cl or F for OH can occur, and as such Cl/OH and F/OH ratios in biotite and amphibole can yield information regarding the concentrations of these ligands at the time of mineral crystallization. However, because of coupled substitution mechanisms, halogen concentrations in the mineral need not directly reflect concentrations in the fluid. Further, significant analytical problems exist with respect to determining fluorine concentrations, and as a consequence, fluorine concentrations were not analysed in this study.

6.4.1 Feldspar chemistry

Feldspar compositions are presented in a ternary orthoclase-albite-anorthite plot in Figure 6.9a. Meta-sedimentary hosted metasomatic feldspars in the Eastern Succession are predominantly albite with a narrow range in composition from Ab_{100} to Ab_{95}. Igneous and igneous-hosted metasomatic plagioclase record a broader compositional range from Ab_{100} to Ab_{48}. Metasomatic potassium feldspars range from Or_{99} to Or_{81} and igneous potassium feldspar ranges between Or_{100} and Or_{89}. Metamorphic feldspar in the Corella Formation is predominantly K-feldspar, with Or_{97} to Or_{81}.

6.4.2 Clinopyroxene chemistry

Complete solid solution exists between the clinopyroxene end members diopside ($CaMgSi_2O_6$) and hedenbergite ($CaFeSi_2O_6$). Eastern Succession clinopyroxene from metamorphic, igneous and both igneous- and metasedimentary-hosted metasomatic assemblages are predominantly diopsidic (Fig. 6.9b) with Di_{35}^{min}, $Di_{78}^{average}$ and Di_{92}^{max}. The overlapping nature of clinopyroxene compositions from these different associations precludes use of the available data as a tracer for variations in fluid chemistry.

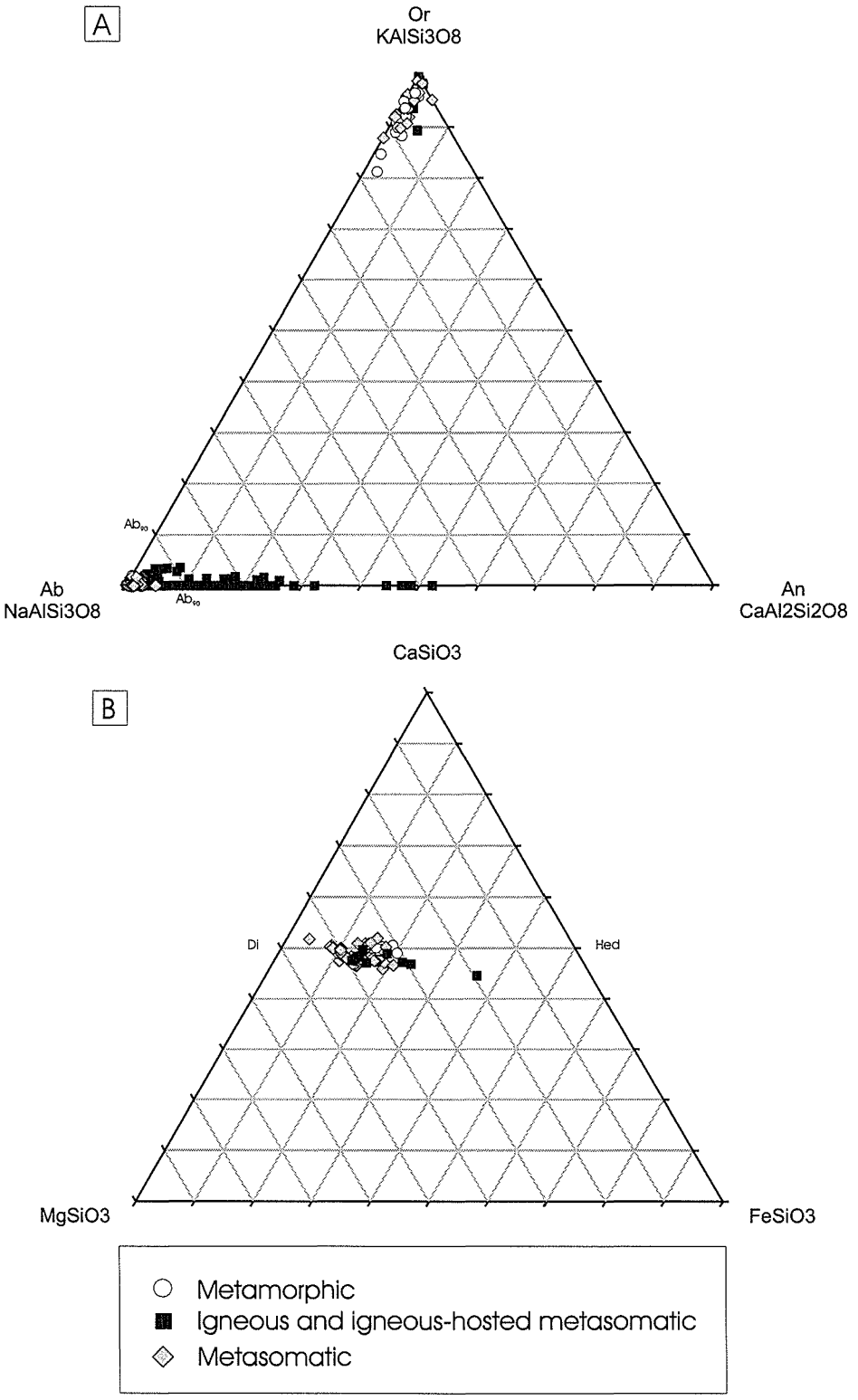

FIGURE 6.9.
Ternary plots for (a) feldspar and (b) pyroxene compositions.

6.4.3 Amphibole chemistry

Amphiboles are a complex group of double chain silicates with the general formula:

$$A_{0-1}B_2C_5T_8O_{22}(OH)_2$$

Stoichiometric recalculation of amphibole analyses has been carried out on an anhydrous basis (23 oxygens), and recalculation of ferric iron was done following the method of Holland and Blundy (1994). Amphibole analyses that were not stoichiometric using the criteria of this method were discarded. Cation site allocations were made on the basis of 24 oxygens, and subsequent classification of amphiboles followed the terminology and methods of Leake et al. (1997).

Nearly all of the amphiboles analysed in this study are calcic amphiboles, [$(Na+Ca)_B \geq 1.00$ and $Na_B<0.50$], with a small number of analyses extending into the sodic-calcic [$(Na+Ca)_B \leq 1.00$ and Na_B in the range 0.50 and 1.50] and sodic [$Na_B \geq 1.50$] fields. All calcic amphiboles are plotted in Figure 6.10.

Metamorphic amphiboles from Corella Formation calc-silicate rocks in the MKFB range from magnesiohornblende to ferrotshermakite, edenite, ferro-edenite, pargasite and ferropargasite (Fig. 6.10). These analyses overlap somewhat with compositions of magmatic amphiboles from the Cloncurry District that range predominantly from magnesiohornblende to edenite, with some spread into the ferro-edenite and pargasite fields. Igneous-hosted metasomatic amphiboles, including inferred magmatic-hydrothermal interface minerals fall within the actinolite field. Metasedimentary-hosted metasomatic amphiboles are also predominantly actinolite, with lesser magnesiohornblende, tremolite and ferro-actinolite (Fig. 6.10). A small number of amphiboles associate with Transitional mineral assemblages are sodic-calcic (winchite and ferrowinchite) and sodic (magnesioriebeckite).

All amphibole compositions are plotted in Figure 6.11. Two main amphibole populations are clearly distinguished on the basis of Si concentrations. These are

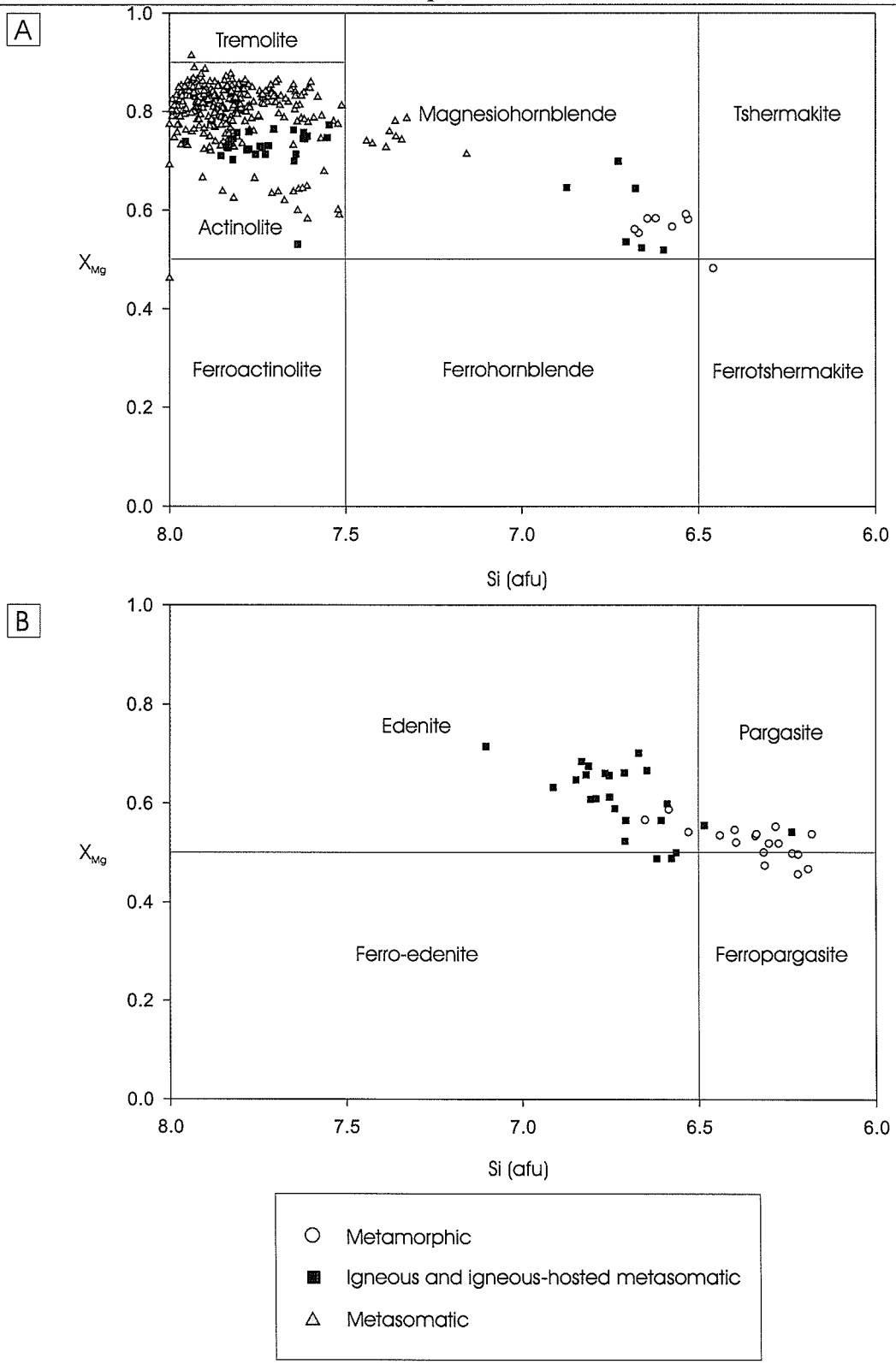

FIGURE 6.10.
Classification of calcic amphiboles, following the scheme of Leake et al. (1997). (a) $(Na + K)_A<0.50$ and $(Ca)_A<0.50$. (b) $(Na+K)_A\geq0.50$ and $Ti<0.50$.

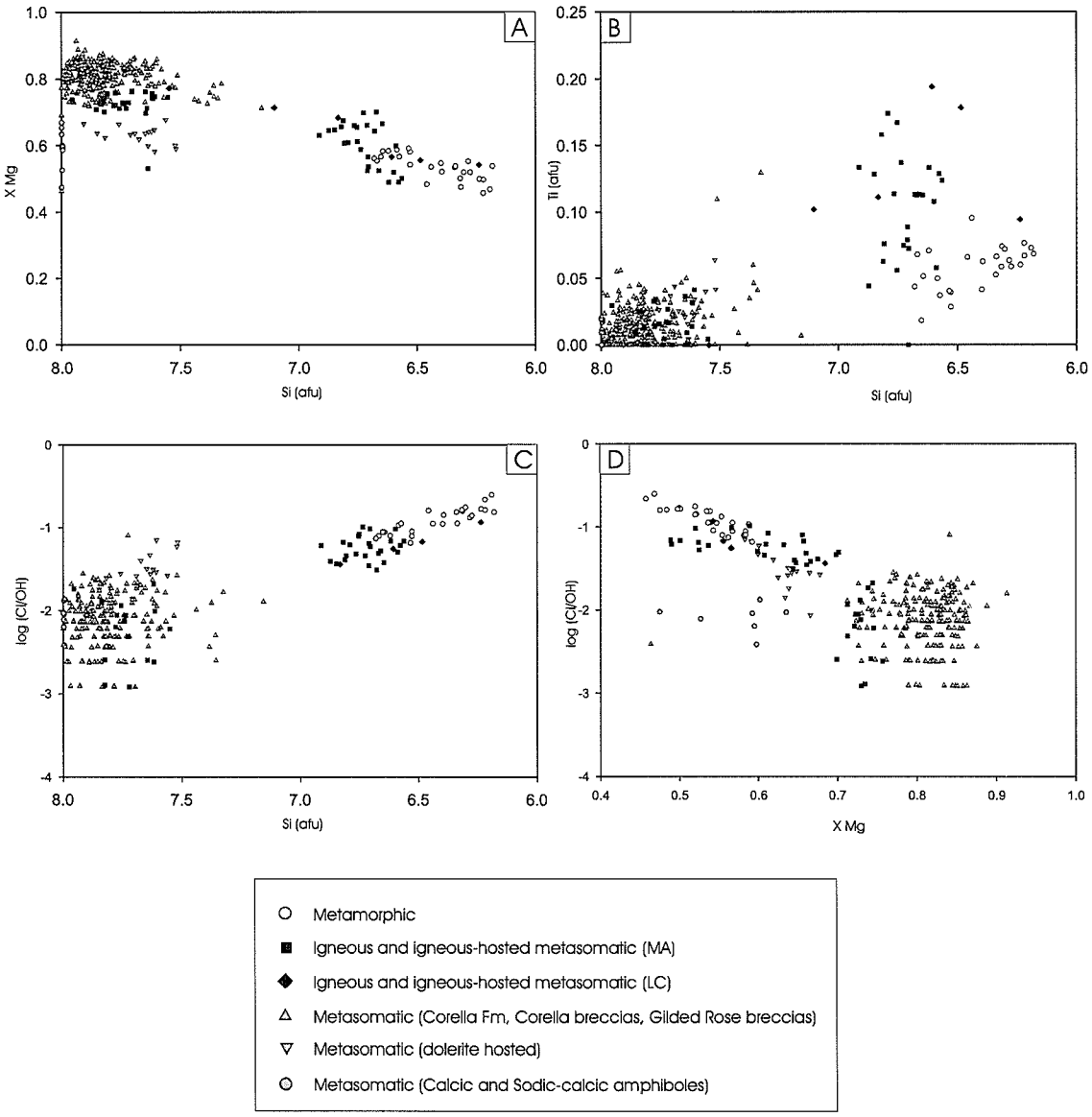

FIGURE 6.11.
Compositional fields of all amphiboles. (a and b) Si concentrations reveal two main amphibole populations, likely reflecting temperature. Metamorphic and igneous amphiboles contain low Si concentrations, and metasomatic (including igneous-hosted metasomatic) amphiboles contain high Si concentrations. (c and d) Metasomatic amphiboles at constant Si and X_{Mg} values indicate a wide range in $\log(X_{Cl}/X_{OH})$, in part reflecting varying fluid chemistry.

magmatic and metamorphic amphiboles at less than approximately 7.1 afu Si, and metasomatic amphiboles at greater than 7.1 afu Si. Si concentrations of amphiboles can be used as rough estimates of crystallization temperatures (e.g. Anderson and Smith, 1995; Ernst and Liu, 1998), with increasing Si incorporated at lower temperatures. However, Si concentrations are also controlled by Al content, and as such variations in Si content evident in Figure 6.11 likely reflect cooling and/or the availability of Al at the precipitation site.

Analyses from igneous-hosted metasomatic actinolite from Mt Angelay and Lightning Creek overlap with analyses from regional alteration (Figs. 11a and 11b). However, actinolite from regional alteration also extend to higher Si concentrations, and may indicate cooling in some samples relative to actinolite precipitated at the magmatic-hydrothermal interface. Magmatic-hydrothermal interface actinolite displays a narrow range in X_{Mg} from ca. 0.69 to 0.77, with a single outlier at 0.53 (Fig. 6.11a). In contrast, meta-sedimentary hosted actinolite records a distinct increase in X_{Mg}, while analyses from a dolerite-hosted vein exhibit decreased X_{Mg}. These variations in X_{Mg} are inferred to reflect local wallrock controls on mineral chemistry.

There is no calibrated method by which to directly relate X_{Cl}/X_{OH} in amphiboles to fluid chemistry, although empirical calculations are possible by comparison with biotite-fluid equilibria (e.g. Oliver et al., 1992). However, for chemically similar amphiboles that formed at similar temperature and pressure conditions, $X_{Cl}/X_{OH}^{amphibole}$ should to some degree reflect $aH_2O/aHCl$ of the fluid or melt from which it crystallised. In Figures 6.11c and d, $\log(Cl/OH)^{amphibole}$ is plotted against two measures of mineral chemistry, Si and X_{Mg}. As noted above, Si concentrations can also provide a rough indication as to crystallization temperature. When examining log(Cl/OH) values over a narrow range in Si or X_{Mg}, it is evident that igneous and metamorphic amphiboles record a relatively narrow range in log(Cl/OH) that either reflects homogenous X_{Cl}/X_{OH} in the source melt or host metamorphic rock, or poor sensitivity of X_{Cl}/X_{OH} in high temperature amphiboles as a measure of fluid composition. Notably, metamorphic amphibole analysed here are from a single calc-silicate layer, while Oliver et al. (1992) documented significant

variations in aNaCl for fluid in equilibrium with different calc-silicate rock layers in the Corella Formation at a given location, indicating metamorphic fluid compositions were strongly rock-buffered. The similarity in X_{Cl}/X_{OH} for igneous amphiboles from both Mt Angelay and Lighting Creek is notable as both these intrusive complexes are intimately associated with widespread alteration, and have been inferred as sources for metasomatic fluids.

In contrast to purely igneous amphibole, magmatic-hydrothermal actinolite exhibits a wide range in X_{Cl}/X_{OH}, at constant values of Si or X_{Mg}. Although this to some degree reflects poor analytical precision at low concentrations of Cl, it also likely reflects some variation in fluid X_{Cl}/X_{OH}. This range in X_{Cl}/X_{OH} is mimicked by actinolite from regional alteration assemblages. Assuming that variations in actinolite X_{Cl}/X_{OH} ratios at constant X_{Mg} in part reflect variations fluid chemistry, both magmatic-hydrothermal and purely metasomatic actinolite were precipitated from fluids that had a range in $a H_2O/a HCl$.

6.4.4 Biotite Chemistry

Biotite is a mica group phyllosilicate with general formula:

$$K_2(Fe^{2+},Mg)_{6-4}(Fe^{3+},Al^{vi},Ti)_{0-2}[(Si_{6-8}Al_{0-2})O_{20}](OH)_4$$

Stoichiometric recalculation of biotite analyses has been carried out on an anhydrous basis (22 oxygens) with no attempt made to estimate Fe^{3+} concentrations. Recalculated microprobe totals (measured probe total + calculated H_2O content – Cl oxygen equivalents) cluster around 100%, and range downwards to ca. 88% in visibly chloritised biotite grains (Fig. 6.12a). Chloritised biotite also records depleted K concentrations. In an attempt to minimize the effects of analytical error and chloritisation on the dataset, analyses with recalculated totals >103% or <97%, and/or K concentrations <1.5afu atomic formula units have been disregarded in the following interpretations.

Biotite X_{Mg} values have been calculated as Mg / (Mg + Fe + Al^{vi}), and are not expected to vary significantly from values calculated using Fe^{2+} as opposed to

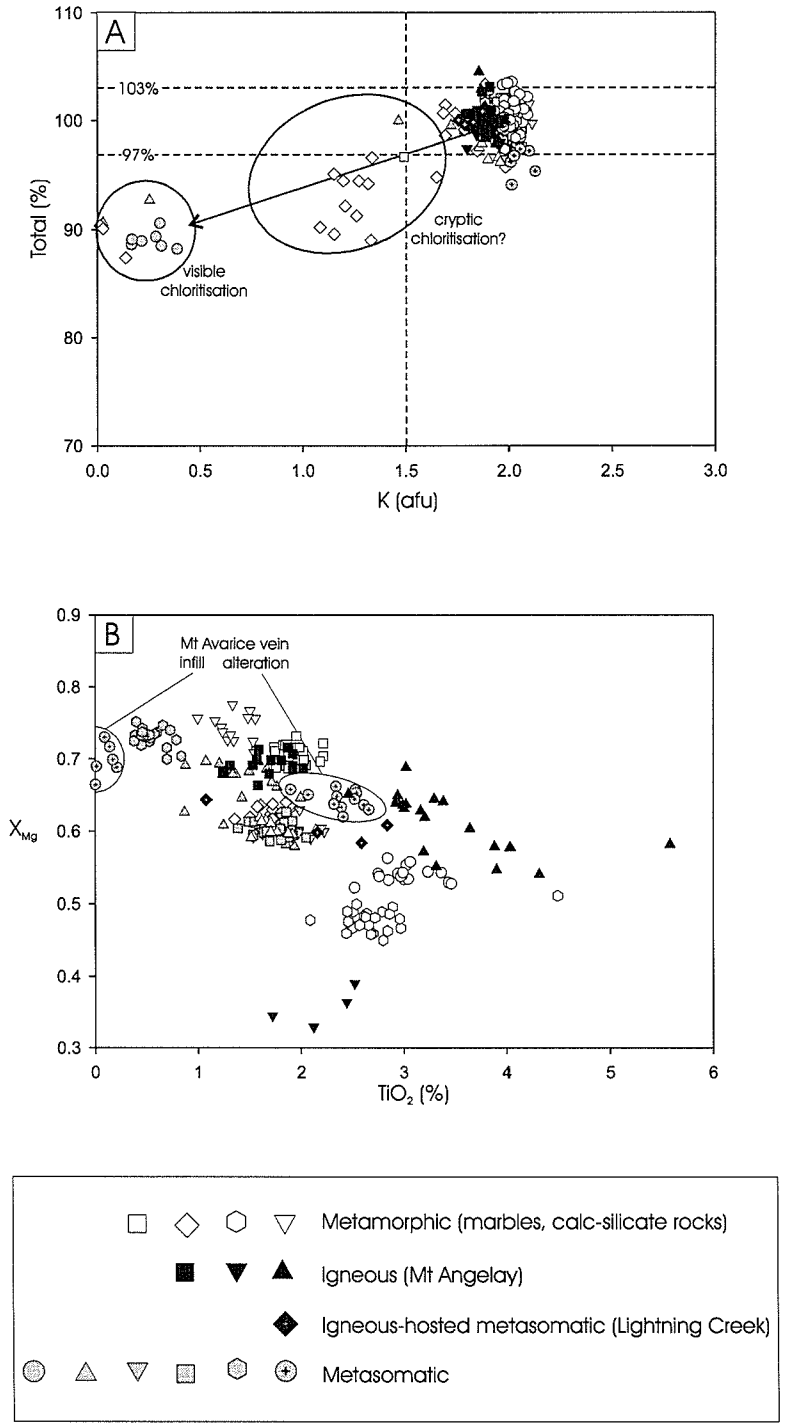

FIGURE 6.12.
Compositional fields for biotite analyses. (a) Visibly choritised biotite records depleted K concentrations and low recalculated probe totals. Analyses at totals >103% or less than 97% and/or K concentrations below 1.5afu have been discarded in subsequent interpretations. (b) TiO_2 concentrations of biotite apparently reflect temperature (ie. magmatic or igneous vs. metasomatic) and availability of Ti at the precipitation site.

total iron. Biotite analyses have X_{Mg} ratios between approximately 0.33 and 0.77 (Fig. 6.12b), well within the range for most naturally occurring biotite (Deer et al., 1992). TiO_2 concentrations are predominantly below 4% with some analyses nearing 6%. The TiO_2 concentration of biotite has been considered as an approximate guide to temperature of crystallization (e.g. Jacobs and Parry, 1976), and this is evident to some degree in Figure 6.12b where magmatic and metamorphic biotite has generally greater TiO_2 concentrations than metasomatic biotite. However, analyses from infill within a single vein at the Mt Avarice quarry record distinctly lower TiO_2 concentrations than metasomatic biotite in the vein's immediate alteration halo. This suggests that the availability of Ti at the precipitation site has a fundamental control on the TiO_2 content of metasomatic biotite, and precludes the use of TiO_2 concentrations in the metasomatic samples as a reliable geothermometer.

The concentration of Cl in biotite is believed to be predominantly controlled by fluid composition (e.g. aH2O/aHCl), $X_{Mg}^{biotite}$, temperature and pressure (Zhu and Sverjensky, 1992; Munoz, 1992). The empirical equation of Munoz (1992) is employed here in order to estimate $\log(fH_2O/f\text{HCl})$ ratios of water-HCl^0 (equivalent to activity ratios at standard state) from biotite chemistry:

$$\log(f\text{H2O}/f\text{HCl}) = [1000/(T(1.15+0.55(X_{Mg}^{biotite})))]+0.68-\log(X_{Cl}/X_{OH})^{biotite}$$

Figure 6.13 presents plots of $\log(X_{Cl}/X_{OH})^{biotite}$ vs. X_{Mg} for Eastern Succession biotite, and distinct clusters are clearly visible for individual samples. For each sample cluster, mean X_{Mg} (where $X_{Mg} = Mg / (Mg + Fe + Al^{vi})$) and mean $\log(X_{Cl}/X_{OH})^{biotite}$ values have been calculated. Using these mean values, as well as mean temperature estimates, $\log(a\text{H2O}/a\text{Cl})$ values have been calculated for each sample cluster (Table 6.4).

Curves representing $\log(a\text{H2O}/a\text{Cl})$ values that correspond with different sample clusters have also been plotted in Figure 6.13 as a function of X_{Mg}, and for the minimum and maximum temperature estimates for the corresponding sample. Spread in biotite analyses parallel to the calculated $\log(a\text{H2O}/a\text{Cl})$ curves in Figure

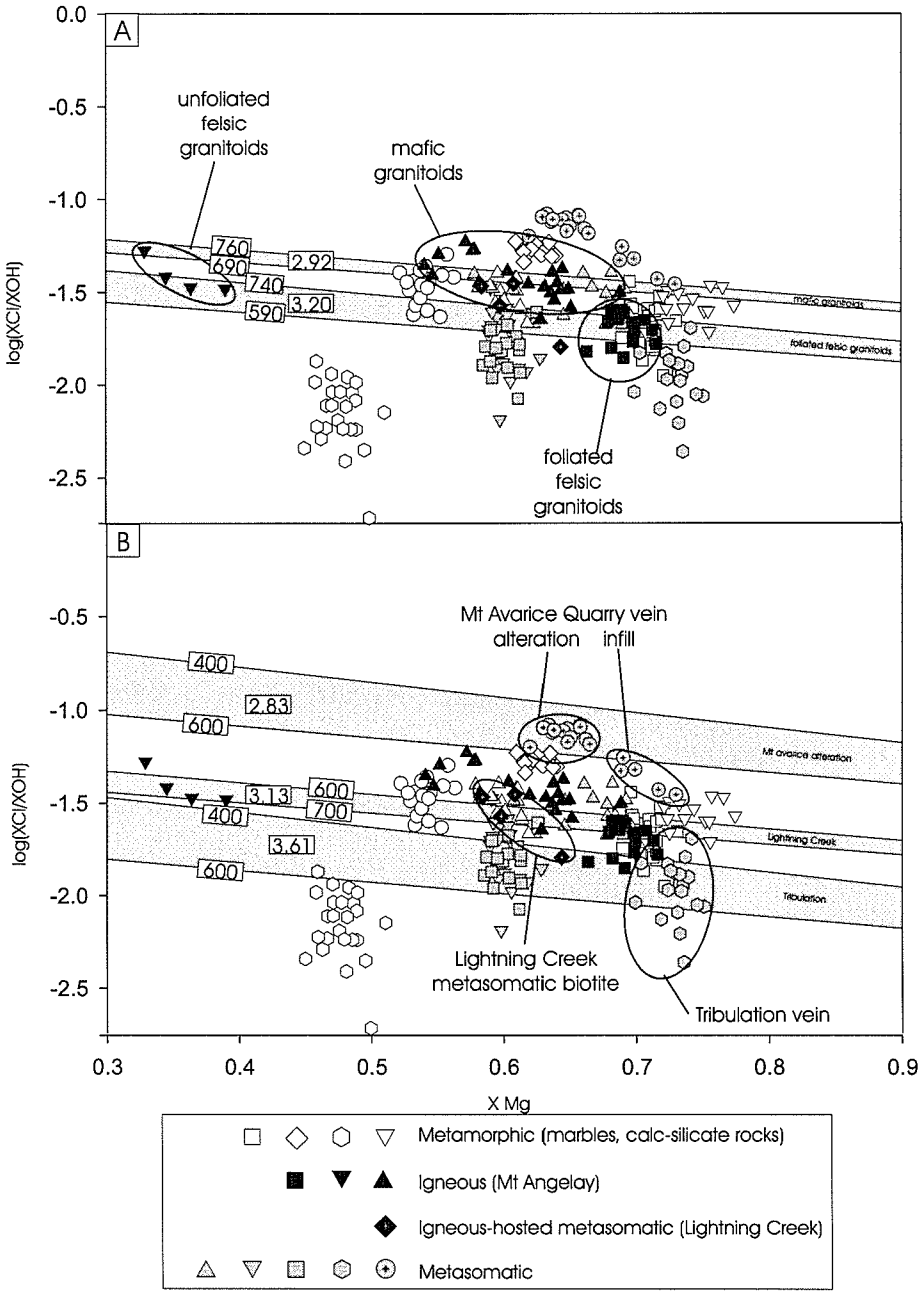

FIGURE 6.13.
$\log(X_{Cl}/X_{OH})$ vs. X_{Mg} plots for Eastern Succession biotite. $\log(aH_2O/aHCl)$ values (e.g. 2.92, 3.20 etc.) are calculated for fluids in equilibrium with the mean log (X_{Cl}/X_{OH}) and X_{Mg} values for different sample clusters, using an intermediate temperature estimate for that sample (e.g. 500°C for Na-(Ca) assemblages). Shaded fields have been plotted for the calculated $\log(aH_2O/aHCl)$ values using the maximum and minimum temperature estimates for that sample (e.g. 400° and 600°C for Na-(Ca) assemblages). (a) $\log(X_{Cl}/X_{OH})$ values calculated for mafic granitoids (2.92, 690°-760°C), and foliated felsic granitoids (3.20, 590°-740°C) from the Mt Angelay igneous complex. (b) $\log(X_{Cl}/X_{OH})$ values calculated for biotite alteration adjacent to a crackle vein at the Mt Avarice quarry (2.83, 400° to 600°C), metasomatic biotite at Lightning Creek (3.13, 600° to 700°C) and biotite from the Tribulation vein (3.61, 400° to 600°C). See text for further discussion.

6.13 can be explained by crystal chemical effects, while variations away from the curves must reflect differences in either temperature or $aH_2O/aHCl$. Where biotite analyses define a field with a span greater than that defined by log(aH2O/aCl) curves calculated over the likely temperature range for the sample, then the data reflects variations in fluid $aH_2O/aHCl$.

Metamorphic biotite records relatively tight and distinct clusters in $\log(X_{Cl}/X_{OH})$ vs. X_{Mg} space (Fig. 6.13), and indicate significant variations in $aH_2O/aHCl$ between samples. This observation is consistent with the findings of Oliver et al. (1992) who indicated strong rock-buffering of $aH_2O/aHCl$ ratios reflecting the original halite content of marble and calc-silicate rock layers in the Corella Formation.

Igneous biotite from the Mt Angelay igneous complex records a wide range in TiO_2 content, and X_{Mg}. Mark (1998) reported solidus temperature estimates from both Ti in biotite and Al in hornblende geothermometers. These range from 415° to 730°C for unfoliated felsic granitoids, 590° to 740°C for foliated felsic granitoids and 690° to 760°C for mafic granitoids. The wide range in solidus temperatures, particularly for the unfoliated felsic granitoids was inferred to record subsolidus re-equilibration. Using mean $X_{Cl}^{biotite}$ and $\log(X_{Cl}/X_{OH})$ values, and intermediate temperatures of 572.5°, 665° and 725°C for the unfoliated felsic, foliated felsic, and mafic granitoids respectively, the Munoz (1992) equation yields $\log(aH_2O/aHCl)$ values of 3.11, 3.20 and 2.92. Plotting these calculated $\log(aH_2O/aHCl)$ curves for foliated felsic (3.20) and mafic granitoids (2.92) at their respective temperature ranges (i.e. 590° to 740°C and 690° to 760°C) reveals two distinct fields (Fig. 6.13a). Further, biotite data from the granitoids extends outside of these fields. This indicates that variations in $\log(X_{Cl}/X_{OH})^{biotite}$ cannot solely be explained by temperature or crystal-chemical effects, and that the biotite in the mafic granitoids crystallised at a lower $aH_2O/aHCl$ ratio than biotite in the foliated felsic granitoids. The $aH_2O/aHCl$ conditions during biotite crystallization in the unfoliated felsic granitoids are difficult to constrain due to the large uncertainty in temperature estimates.

At Lightning Creek, Perring et al. (2001) documented sub-solidus (i.e. metasomatic) biotite growth within the Squirrel Hills granite at ca. 600° - 700°C. The data has a mean X_{Mg} of 0.61 and mean $\log(X_{Cl}/X_{OH})$ of –1.57. Calculated $\log(a H_2O/a HCl)$ at 650°C is 3.13. The 600° to 700°C band (calculated at $\log(a H_2O/a HCl) = 3.13$) dissects data from igneous biotite at Mt Angelay, and indicates similar $a H_2O/a HCl$ conditions during biotite crystallization (Fig. 6.13b).

All remaining metasomatic biotite samples in this study are in equilibrium with quartz and actinolite ± magnetite assemblages, for which mineral-pair isotope geothermometry has established temperatures in the range of 400° - 600°C. Using an intermediate temperature of 500°C, $\log(a H_2O/a HCl)$ ratios were calculated from mean X_{Mg} and mean $\log(X_{Cl}/X_{OH})$ values from metasomatic biotite, using the Munoz (1992) equation (Table 6.4). Calculated $\log(a H_2O/a HCl)$ ratios include a minimum value of 2.83 for the alteration halo to a small quartz, calcite, magnetite, actinolite and biotite vein at the Mt Avarice quarry and a maximum value of 3.61 for biotite at the margin of the Tribulation large aperture calcite-rich vein (Fig. 6.13b). Lines representing these greatest and least $\log(a H_2O/a HCl)$ ratios at both 400° and 600°C were plotted as a function of X_{Mg} in Figure 6.13b. The fields defined by these curves do not overlap, indicating that variations in the greatest and least calculated $\log(a H_2O/a HCl)$ ratios from metasomatic biotite cannot be explained by either biotite crystal-chemical effects, or variations in temperature. Thus biotite in the alteration halo to the Mt Avarice vein precipitated from fluids with greater $a HCl$ (or lesser $a H_2O$) than fluids at the Tribulation vein. Notably, carbon and oxygen stable isotope data from these two veins (**Chapter 7**) indicates that the Mt Avarice vein has a "rock buffered" isotopic signature, while the Tribulation vein has a "fluid buffered" isotopic signature.

The Mt Avarice vein alteration halo biotite records a tight cluster in both X_{Mg} and $\log(X_{Cl}/X_{OH})$ values that falls within the 400° to 600°C band defined for a fluid with $\log(a H2O/a HCl)$ of 2.83. In contrast, infill biotite analyses from the associated vein record compositions that extend below the 600°C band (i.e. to lower $\log(X_{Cl}/X_{OH})^{biotite}$ values). This indicates that the $a H_2O/a HCl$ ratio of fluids from which the vein precipitated was greater than that for the fluids from which the

alteration biotite precipitated. Given the close association at this locale between veins and coarse-grained metasomatic biotite in the immediate wallrocks, and the similar infill and alteration assemblages, it seems most likely that the vein-biotite and alteration-biotite precipitated from the same fluid. If this is accepted, then the lower apparent $a\mathrm{H_2O}/a\mathrm{HCl}$ ratio associated with wallrock biotite may reflect a local (wallrock) source for some Cl. In a similar manner, a local source for Ti was also invoked above for alteration-biotite from this sample. Alternatively, $a\mathrm{H_2O}$ may be partly buffered by the wallrock composition.

Biotite analyses from the Tribulation vein define a relatively broad cluster in $\log(X_{Cl}/X_{OH})$ vs. X_{Mg} space, with analyses extending both above and below the 400° to 600°C band calculated for $\log(a\mathrm{H_2O}/a\mathrm{HCl})$ of 3.61 (Fig. 6.13b). This suggests variation in the $a\mathrm{H_2O}/a\mathrm{HCl}$ ratio during biotite precipitation. As suggested above for the Mt Avarice vein, this variation may reflect contrasting $a\mathrm{H_2O}/a\mathrm{HCl}$ in the hydrothermal fluid relative to the wallrock, although in this instance it is not clear whether fluid $a\mathrm{H_2O}/a\mathrm{HCl}$ was increased or decreased through wallrock interaction.

6.5 OXIDE CHEMISTRY

The trace element composition of magnetite and subordinate hematite was analysed in order to further track changes in fluid chemistry associated with varying metasomatic assemblages. Samples were selected to include metamorphic and magmatic magnetite, and magnetite and hematite from a variety of metasomatic assemblages, barren ironstones and the Ernest Henry orebody. The data forms part of a larger dataset including analyses from many of the Cloncurry District iron-oxide-Cu-Au deposits (Carew, in prep.). Controls on the trace element chemistry of magnetite and hematite are poorly understood, but likely reflect fluid, melt or whole rock chemistry (for metasomatic, igneous and metamorphic minerals respectively), temperature and pressure. Further, for metasomatic minerals, chemical variations may also reflect whether mineral growth occurred as infill, or as wall-rock or breccia matrix alteration. This is particularly noted for elements such as Al, Ti and V that are relatively immobile in most hydrothermal fluids. The concentrations of

these elements in metasomatic minerals may be strongly influenced by their concentration at the depositional site, and the rate of diffusion of these elements.

Perhaps the most significant difficulty in measuring magnetite and hematite mineral chemistry is in obtaining pure samples, as these minerals commonly contain inclusions of other minerals. In this study, magnetite and hematite chemistry were determined by laser-ablation inductively coupled plasma mass spectrometry (LA-ICPMS) at Macquarie Univeristy, using a Merchantek LUV266 laser microprobe and Agilent 7500 ICP-MS. The procedure provides a rapid and high-precision method for in situ analysis of mineral chemistry that yields trace element analyses to sub-ppm levels with a precision of <5%. Results have been shown to correlate well with those of the proton microprobe (Norman et al., 1996, 1998). Analyses were normalised to 96 and 94 cation wt. % Fe for magnetite and hematite respectively. The NIST-610 external standard and BCR2G internal reference were employed in data validation and reduction using the Glitter software package. Norman et al. (1996) give detailed descriptions of analytical and calibration techniques.

6.5.1 Magnetite chemistry

While the chemistry of magnetite is commonly close to that defined by its theoretical end-member formula ($Fe^{+2}Fe_2^{+3}O_4$) it can contain appreciable quantities of Al, Cr, Mg, V and Ti substituting for Fe^{+3} and Ca, Mn and Mg substituting for Fe^{+2}. Smaller amounts of Si, Cr, Ni, Co, Zn and Cu have also been reported from magnetite analyses (e.g. Nystrom and Henriquez, 1994, and references therein).

Although detailed petrography was undertaken in selecting large and apparently inclusion-free mineral grains, the penetrative nature of laser ablation means that inclusions below the observed surface may be ablated, affecting the elemental analysis. Of the 39 elements analysed by LA-ICPMS, 15 elements (Mg, Al, Si, P, Ca, Ti, V, Cr, Mn, Fe, Co, Ni, Cu, Zn and Ga) were present in concentrations that were consistently above the instrumental detection limits. Of these, the concentration of Fe was assumed to be constant, and the measured Fe concentrations were used in normalizing the concentrations of other elements. The

normalized concentrations of Mg, Al, Si, P, Ca, Cr and Cu were extremely variable within individual samples, likely reflecting the inclusion of various silicate, carbonate, phosphate, oxide and sulphide minerals. As a consequence, the measured concentrations of these elements do not necessarily reflect magnetite chemistry, and no interpretations have been made on data for these elements. Where large concentrations of the above elements (Mg ≥ 1000ppm, Al ≥ 2000ppm, Si ≥ 10000ppm, P ≥ 50ppm, Ca ≥ 10000ppm, Cu ≥ 20ppm, Cr ≥ 1500ppm) were detected, all data from that analysis was discarded, with the above thresholds being established so as to eliminate obvious outliers in the data. While some remaining analyses may contain smaller inclusions of various minerals, inspection of binary plots indicates that variations in the concentration of the above elements could not explain observed variations in the concentrations of the remaining elements of interest.

For some samples, a number of anomalously high Ti analyses were recorded, and likely reflect the inclusion of ilmenite grains. Samples that record high and variable Ti concentrations also show a weak correlation between Ti and both V and Ga. However, differences in Ti, V and Ga concentrations between samples exceeds that within individual samples, and on the whole, Ti concentrations do not increase in a linear manner with either V or Ga. Thus, while some high Ti-analyses likely reflect the inclusion of ilmenite, and this may have affected V and Ga concentrations to a small degree, this does not appear to have had a significant impact on the dataset as a whole. Also, some samples record one or more anomalously high Co analyses that may record small inclusion of Co-bearing minerals within magnetite. However in general, individual samples record relatively narrow ranges for Ti, V, Mn, Co, Ni, Zn and Ga that with the exception of a small number of outliers are interpreted to reflect magnetite mineral chemistry. Average concentrations of these elements are given in Table 6.5.

LA-ICPMS data indicates that magmatic and hydrothermal magnetite from Mt Angelay is characterized by variable Ti (34 to 1398 ppm) and high but variable V (1455 to 2739 ppm) concentrations (Fig. 6.14). Mn, Ni, Co and Ga concentrations are all relatively low. Magnetite from the Marimo large aperture calcite vein has

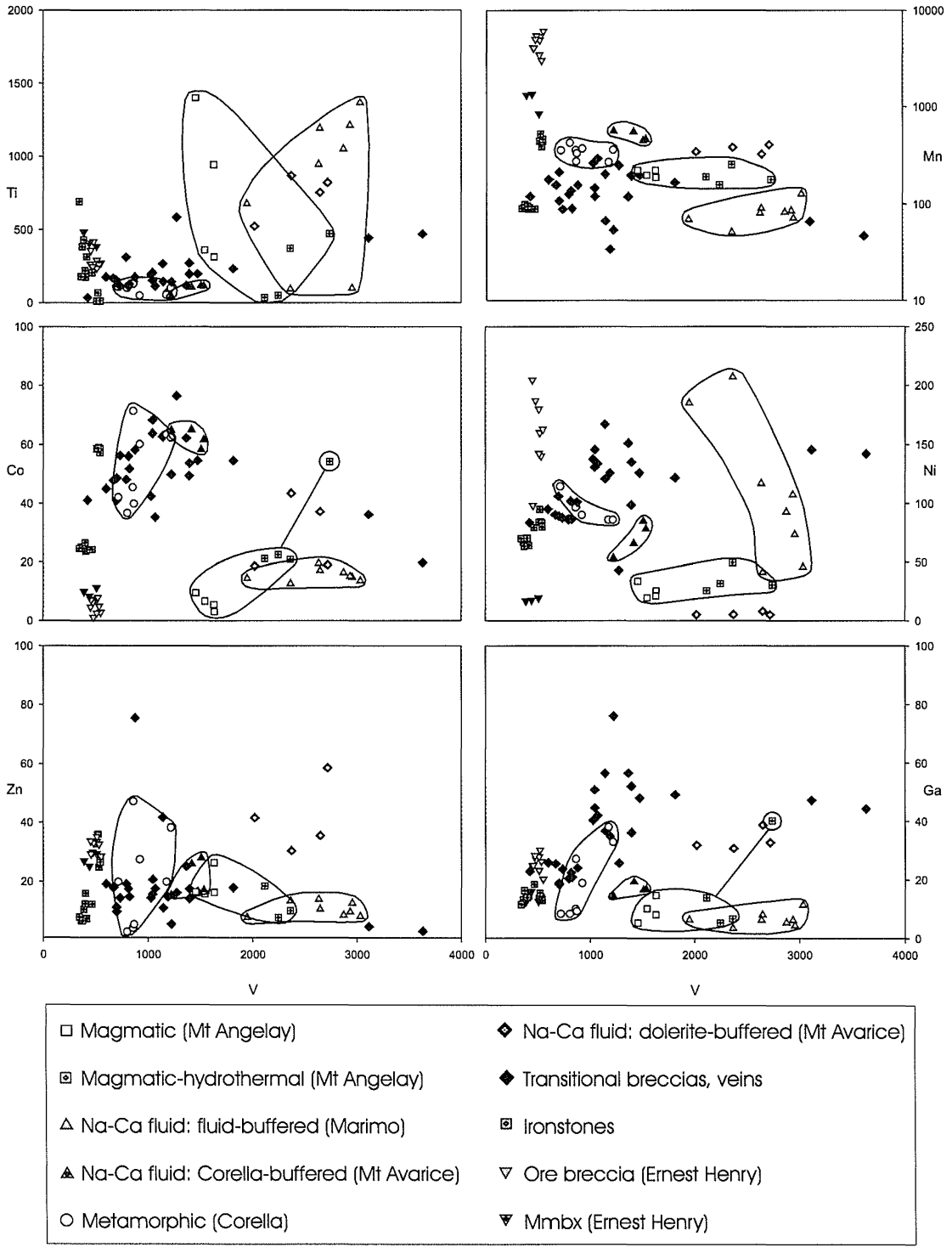

FIGURE 6.14.
Trace element compositions of magnetite grains, determined by LA-ICPMS analysis. All values are in ppm notation. For most elements, Marimo and Mt Angelay samples record similar compositions. Analyses from an apparently rock-buffered vein at the Mt Avarice Quarry records composition that are intermediate between the Marimo / Mt Angelay analyses, and metamorphic magnetite in the Corella Formation.

similar concentrations in Ti (92 to 1364 ppm), Cr, Mn, Co and Ga relative to concentrations recorded in Mt Angelay magnetite. Concentrations of V (1949 to 3033 ppm) and Ni in the Marimo vein magnetite overlap with the Mt Angelay samples, and extend to higher values.

Metamorphic magnetite from Corella Formation calc-silicate rocks has moderate to low V (714 to 1218 ppm) and low Ti concentrations (49 to 142 ppm). The samples also contain low to moderate Ga, moderate Ni and high Co concentrations. Several analyses from a small calcite, quartz, magnetite, actinolite and biotite vein from the Mt Avarice quarry described above with respect to biotite chemistry were undertaken. While this vein has a mineralogy typical of Na-(Ca) alteration systems in the Cloncurry District, the small vein size, a lack of intense albitic wall-rock alteration, and high calcite, actinolite, quartz and magnetite $\delta^{18}O$ values indicate that the vein-forming fluids were to a large extent rock buffered. Analyses from this vein form tight clusters with respect to each of the elements of interest, and element concentrations are typically intermediate between values characteristic of the Mt Angelay / Marimo samples, and metamorphic magnetite from Corella Formation calc-silicate rocks. Magnetite analyses from a dolerite-hosted (quartz, magnetite, actinolite, pyrite) vein, also from the Mt Avarice quarry, records elevated V (2022 to 2722 ppm) and Zn concentrations, and depleted Ni concentrations. These variations may also reflect buffering of fluid chemistry by wallrocks, in this instance dolerite.

Ernest Henry magnetite has a very distinct chemical signature, particularly with respect to low V (388 to 553 ppm) and extremely high Mn (845 to 6065 ppm) concentrations. Notably, analyses from two barren ironstones have similar low V (343 to 544 ppm) concentrations, and may imply a similar origin to magnetite from Ernest Henry. The barren ironstone magnetite however has elevated Co, and lacks the extreme Mn enrichment in Ernest Henry magnetite.

Magnetite analyses from a number of Transitional (actinolite- and chlorite-bearing) to Retrograde (chlorite-bearing) breccias and veins has a wide range in concentrations of most elements, however the bulk of the data overlaps with analyses from metamorphic magnetite.

Implications of variations in magnetite chemistry

The similarity in magnetite chemistry between the Mt Angelay and Marimo samples suggests similar fluid chemistry during mineral precipitation. This is consistent with the inference of Mark and Foster (2000) that the Mt Angelay igneous complex and other similar plutonic bodies in the Eastern Succession may have provided fluids responsible for regional Na-(Ca) alteration. Further, the similarity in magnetite chemistry is consistent with the interpretation that the Marimo and other large aperture calcite veins throughout the Eastern Succession record minimal wallrock interaction. That is, the vein forming fluids were not rock-buffered (see also Oliver et al., 1993; **Chapter 7**, this study). Of the analysed elements, Ti and V are commonly the least mobile in metasomatic fluids. Given the large size of the Marimo vein, and the clear occurrence of the analysed magnetite grains as infill within the vein (and away from the vein's wallrocks), diffusion of Ti and V from the immediate wallrocks is considered unlikely to explain the high concentrations of these elements in this sample. Alternatively, high Ti and V concentrations in the Marimo vein magnetite may indicate that the fluids were saline, and had not cooled significantly from their source.

Magnetite analyses from a small and apparently rock-buffered vein from the Mt Avarice quarry record mineral chemistry that is intermediary between the Mt Angelay / Marimo samples and metamorphic magnetite from Corella Formation calc-silicate rocks. This observation is consistent with isotopic and mineralogic observations that suggest the vein was precipitated from fluids that were buffered by interaction with Corella Formation rocks. Thus the composition of magnetite from this vein may reflect modification of fluid chemistry via wallrock equilibration, away from an original composition similar to fluids from which Mt Angelay and Marimo magnetite precipitated.

The remaining magnetite analyses, from retrograde breccias and veins, ironstones and the Ernest Henry orebody also show depleted Ti and V concentrations relative to the Mt Angelay and Marimo samples, and may indicate magnetite precipitation distal to the fluid source, and/or from lower temperature or

lower salinity fluids. However, geochemical trends for the other elements of interest (Mn, Co, Ni and Zn) are more complex, and may reflect a number of processes including cooling, fluid unmixing, equilibration with wallrocks other than the Corella Formation, or input of fluids from different sources. Ernest Henry magnetite in particular is chemically distinct with low V and extremely high Mn concentrations. The high Mn concentrations are unique to the Ernest Henry analyses and their significance remains unexplained, although it is noted that the Ernest Henry ore system in general is enriched in Mn, relative to its hostrocks (Mark et al., 2001).

6.5.2 Hematite chemistry

A limited LA-ICPMS investigation of hematite grains from Transitional to Retrograde breccias and hematite-rich ironstones was undertaken. Analyses with significant Mg, Al, Si, P, Ca, Cu and/or Cr contamination were eliminated from the dataset, as was done for magnetite analyses above. The remaining samples exhibit a very large range in Ti concentrations (6 to 12674 ppm) up to an order of magnitude greater than recorded in the magnetite samples. High Ti values are interpreted to reflect inclusion of ilmenite grains that were noted petrographically in some samples. V and Ga show strong correlation with Ti concentrations and may also record contamination by ilmenite. Given the apparent large degree of contamination within hematite grains, and the influence of this on several elements, no further interpretation was carried out on hematite mineral chemistry.

6.6 DISCUSSION

Regional alteration assemblages developed within Mary Kathleen Group stratigraphy in the Eastern Succession, as documented in this contribution, can be divided into three broad associations. Na-(Ca) alteration is characterized by albite and actinolite ± quartz, calcite, magnetite, diopside, scapolite, apatite, biotite, titanite and local sulphide-bearing assemblages. Transitional assemblages contain calcite, quartz and both amphibole (actinolite, Na-Ca- or Na-amphibole) and chlorite ± K-feldspar, biotite, hematite, magnetite, epidote, muscovite, fluorite,

tourmaline, and locally sulphides. Retrograde assemblages lack amphibole, and contain calcite, quartz and chlorite bearing assemblages.

Na-(Ca) metasomatic assemblages are similar to those developed in inferred magmatic-hydrothermal interface rocks within various plutonic complexes of the Eastern Succession. Temperatures for Na-(Ca) alteration within the Corella Formation are predominantly between 400° and 600°C, and amphibole chemistry likely indicates some cooling relative to igneous hosted metasomatic amphibole. Further, overlapping $\delta^{18}O$ values from mineral separates are consistent with a similar origin for meta-sedimentary-hosted and igneous-hosted metasomatic assemblages. While the isotopic data does not unequivocally indicate magmatic fluid sources, as opposed to fluids equilibrated with magmatic rocks, tight clustering of isotope data from magmatic and igneous hosted metasomatic minerals is most consistent with magmatic fluid sources. Unequivocal support for magmatic fluid sources is presented in **Chapter 7**.

Magnetite chemistry from large aperture calcite veins is very similar to chemistry recorded by magmatic-hydrothermal interface magnetite, and suggests that the large aperture veins record precipitation under fluid-buffered conditions. In the more distal portions of Na-(Ca) alteration systems, magnetite mineral chemistry approaches that defined by metamorphic magnetite, and may indicate buffering of fluid composition by interaction with metamorphic rocks. This buffering is also reflected in both increases and decreases in $X_{Mg}^{actinolite}$, varying with rock type, and by a shift in mineral separate $\delta^{18}O$ values towards higher ratios that are typical of least altered metamorphosed marine carbonates of the Corella Formation (see **Chapter 7**). Mineral separate stable isotope data from most Cu±Au ore deposits in the Eastern Succession also records shifts to higher $\delta^{18}O$ values relative to igneous assemblages, again likely reflecting interaction with isotopically heavier wallrocks. This is particularly noted for ore proximal K-feldspar that shows an increase in $\delta^{18}O$ ratios relative to both albite in regional alteration assemblages, and relative to igneous feldspars. These observations are consistent with the model of Oliver et al. (in revision), whereby magmatic fluids become progressively enriched in KCl and

FeCl, eventually stabilizing K-feldspar and biotite, as a result of stripping K and Fe from wallrocks during albitisation.

The chlorine content of biotite from igneous and igneous hosted metasomatic assemblages from both Mt Angelay and Lightning Creek indicates fluids of moderate salinity, with calculated $\log(a\mathrm{H_2O}/a\mathrm{HCl})$ values from 3.20 to 2.92. This range in salinity cannot be explained by temperature variations or crystal chemical effects, and indicates variations in salinity between different magmatic phases. This highlights the potential of using the chlorine content of biotite in discriminating different plutons or magmatic phases as possible sources of saline brines (e.g. Cleverley et al., 2000; Coulson et al., 2001).

Relative to igneous biotite, metamorphic biotite within the Corella Formation exhibits a wide range in calculated $\log(a\mathrm{H_2O}/a\mathrm{HCl})$ ratios between 3.99 and 2.99. Similarly, Corella-hosted metasomatic biotite exhibits a wide range in $\log(a\mathrm{H_2O}/a\mathrm{HCl})$ ratios from 3.61 to 2.83. If magmatic fluid sources are inferred for metasomatic biotite, then the available data suggests both increases and decreases in $a\mathrm{H_2O}/a\mathrm{HCl}$ from source to metasomatic biotite precipitation. Unmixing of $\mathrm{H_2O}$-$\mathrm{CO_2}$-NaCl fluids provides one mechanism for such a decrease, while dilution with less saline fluids would result in an increase in $a\mathrm{H_2O}/a\mathrm{HCl}$. In addition, in one instance documented here, $\log(a\mathrm{H_2O}/a\mathrm{HCl})$ ratios calculated from metasomatic biotite in a vein's alteration halo are lower (i.e. greater $a\mathrm{HCl}$, or lower $a\mathrm{H_2O}$) than for infill biotite in the associated vein. This may indicate a component of locally derived chlorine. A large spread in $\log(X_{Cl}/X_{OH})$ ratios for the associated infill cannot be explained by crystal chemical or temperature effects and also likely reflect variations in $(a\mathrm{H_2O}/a\mathrm{HCl})^{fluid}$, again possibly indicating some chlorine sourced from the local wallrocks. One mechanism for this is by the replacement of metamorphic scapolite by albite, releasing chlorine into a metasomatic fluid, although the breakdown of other Cl-bearing metamorphic minerals (i.e. biotite and amphibole, where present) is also possible, and indeed albitisation in the Eastern Succession is commonly biotite-destructive. Oliver et al. (in revision) previously addressed this concept, with respect to evaporitic chlorine sequestered into metamorphic scapolite in the Corella Formation acting as a source for metasomatic

salt. As illustrated in the following reaction equation from Oliver et al. (in revision), releasing chlorine into a metasomatic fluid, for example by the breakdown of scapolite of intermediate composition to albite, requires an already saline fluid:

$$Na_{12}Ca_8Si_{40}Al_{20}O_{120}Cl_3(CO_3)_2 + 20\ SiO_2 + 8\ NaCl + 5\ HCl \rightarrow$$
$$20\ NaAlSi_3O_8 + 8\ CaCl_2 + 2\ CO_2 + 2\ H_2O + 0.5\ H_2$$

While Oliver et al. (in revision) used the above observations to discount the metamorphosed Corella Formation as a significant source of metasomatic salt, chlorine contents of metasomatic biotite presented in this study indicate that fluids can become progressively more saline through wall rock interaction. However, as noted by Oliver et al. (in revision) an initially saline fluid is still required.

6.7 CONCLUSIONS

Combined, observations from metasomatic mineral assemblages and mineral and isotope chemistry presented in this contribution yield further support for models which invoke magmatic sources for metasomatic fluids in the Eastern Succession. In particular, tight clustering of isotopic ratios for igneous and igneous-hosted metasomatic minerals is most consistent with magmatic fluid sources as opposed to fluids being partially equilibrated with magmatic rocks. Further, similarities in trace element chemistry for magmatic-hydrothermal interface magnetite and magnetite in large aperture calcite veins indicate similar fluid chemistry, and ambient precipitation condition. Plutonic rocks in the Eastern Succession have been shown by other authors to be capable of producing already saline metasomatic fluids (e.g. Perring et al. 2000), and fluid unmixing has been appealed to as a mechanism for further increasing fluid salinity (Pollard, 2001). In this contribution, evidence from biotite chemistry suggests that wallrock interaction, including the replacement of scapolite by albite has the potential to further increase metasomatic fluid salinity.

CHAPTER 6 TABLES

Table 6.1 Data sources

Association	Location		Stable isotopes: Magnetite	Hematite	Quartz	Albite	K-feldspar	Actinolite	Chemistry: Feldspar	Pyroxene	Actinolite	Biotite	Sources
Igneous & igneous hosted metasomatic	Lightning Creek	LC	X		X	X			X	X	X	X	Perring et al. (2000, 2001)
	Bull Creek	BC			X								Munro (1997)
	Mt Margaret	MM			X		X						Pollard et al. (1997b)
	Saxby Granite	SG			X		X						Pollard et al. (1997b)
	Mt Angelay & Roxmere Pluton	MA	X		X	X	X	X	X	X	X	X	Pollard et al. (1997b); Darvall (1998); Tolman (1998); Mark & Foster (2000)
Regional alteration	THIS STUDY	TS	X	X	X	X		X	X	X	X	X	Tables 2 and 3, this study
	Mt Angelay environs	MA	X	X	X	X	X	X	X	X	X		Mark (1998a)
	MFC volcanics	MFC	X		X			X					Blake et al. (1997)
	Maramungee	Mrmg			X			X					Pollard et al. (1997b)
	Fullarton River	FR						X					Pollard et al. (1997b)
Cu-(Au) ore and ore proximal alteration	Mt Elliott	ME	X					X		X	X		Little (1997); Pollard et al. (1997c)
	Ernest Henry	EH	X	X	X		X	X					Mark et al.(1999); Twyerould (1997)
	Tick Hill	TH	X		X	X							Choy (1994)
	Starra	St	X	X	X								Rotherham et al. (1998)
	Southern Extensions	SE	X					X					Pollard et al. (1997c)
	Little Eva	LE	X										Pollard et al. (1997c)
	Great Australia	GA			X								Cannell & Davidson (1998)
	Eloise	El			X			X					Baker et al. (2001)
	Mt Dore	MD			X		X						Beardsmore (1992)
	Bull Creek	BC			X								Munro (1997)
	Plume	Pl						X					Pollard et al. (1997c)
	Houdini	Hd				X							Weston (2000)
	Osborne	Os	X		X	X							Adhsead (1995); Pollard et al. (1997); French (1997)

Table 6.2. Mineral separate stable isotope data

Area	Rock type	Sample #	mag	hem	qtz	alb	act
Budenberri	Na-(Ca) breccia	Bud42	3.4				8.0
Camel Hill	Ironstone	1561a		0.6			
	Transitional breccia	1561b		-0.1			9.8
Cloncurry region	Retrograde breccia	345	6.9				
Gilded Rose	Transitional breccia	1307	5.4				9.7
	Transitional breccia	1314	5.3		14.3		
	Transitional breccia	1310a					9.3
	Transitional breccia	1351a	4.1	-0.6	14.7		
	Ironstone	1356a	4.9	1.1			
Mt Avarice	Na-(Ca) vein	1375.04	10.0		19.1		15.9
	Multistage vein	1375.06d	0.7	-5.3	12.8		7.6
Roxmere-Marimo	Na-(Ca) breccia	1808	3.7				9.4
	Na-(Ca) vein	1384b	3.4				9.6
Tribulation	Na-(Ca) altered pegmatite	T72B			11.7		
	Na-(Ca) vein	T72C				8.4	12.0
	Na-(Ca) altered calc-silicate	T72e					7.4
	Na-(Ca) vein	T72f					9.6
	Na-(Ca) breccia	T72g				9.3	8.2

All values in ‰ $\delta^{18}O$ notation relative to V-SMOW.

Table 6.3a. Representative microprobe analyses: Feldspar

	Gilded Rose				Roxmere-Marimo			Budenberri		Cloncurry Region			
	alteration				alteration			alteration		metamorphic			
	1351a	1374	1307	1314	1384b	1808	1714	Bud42	Bud67	1047	1394	0606b	0607b
SiO2%	69.13	68.32	63.39	63.43	70.14	68.96	69.36	70.32	70.47	63.51	63.58	63.19	64.13
TiO2%	0.12	0.24	0.30	0.00	0.00	0.00	0.00	0.00	0.21	0.49	0.04	0.12	0.11
Al2O3%	18.91	18.89	17.23	16.91	19.23	18.81	18.55	19.28	18.69	17.61	17.54	17.79	17.36
FeO%	0.90	0.00	0.00	0.33	0.19	0.12	0.10	0.34	0.08	0.32	0.00	0.10	0.60
MnO%	0.00	0.00	0.14	0.03	0.13	0.08	0.00	0.00	0.14	0.24	0.00	0.00	0.16
MgO%	0.23	0.00	0.00	0.43	0.28	0.01	0.20	0.19	0.00	0.55	0.03	0.52	0.20
CaO%	0.00	0.20	0.00	0.52	0.20	0.00	0.09	0.03	0.23	0.58	0.48	0.06	0.21
Na2O%	10.79	10.52	0.94	0.66	9.92	10.31	10.80	10.55	10.96	0.93	1.96	0.07	0.25
K2O%	0.14	0.00	16.14	16.41	0.24	0.04	0.13	0.20	0.09	14.35	14.71	16.46	16.19
TOTAL%	100.22	98.16	98.14	98.71	100.33	98.33	99.23	100.91	100.87	98.56	98.34	98.31	99.21
Atomic Formula Units (afu)													
Si	3.01	3.02	3.00	3.00	3.03	3.04	3.04	3.03	3.04	2.97	2.99	2.98	3.00
Ti	0.00	0.01	0.01	0.00	0.00	0.00	0.00	0.00	0.01	0.02	0.00	0.00	0.00
Al	0.97	0.98	0.96	0.94	0.98	0.98	0.96	0.98	0.95	0.97	0.97	0.99	0.96
Fe	0.03	0.00	0.00	0.01	0.01	0.00	0.00	0.01	0.00	0.01	0.00	0.00	0.02
Mn	0.00	0.00	0.01	0.00	0.00	0.00	0.00	0.00	0.01	0.01	0.00	0.00	0.01
Mg	0.01	0.00	0.00	0.03	0.02	0.00	0.01	0.01	0.00	0.04	0.00	0.04	0.01
Ca	0.00	0.01	0.00	0.03	0.01	0.00	0.00	0.00	0.01	0.03	0.02	0.00	0.01
Na	0.91	0.90	0.09	0.06	0.83	0.88	0.92	0.88	0.92	0.08	0.18	0.01	0.02
K	0.01	0.00	0.97	0.99	0.01	0.00	0.01	0.01	0.00	0.86	0.88	0.99	0.97
Total	4.96	4.93	5.04	5.06	4.90	4.91	4.94	4.93	4.94	4.99	5.05	5.02	5.01
Or	0.8	0.0	91.9	92.0	1.5	0.3	0.8	1.2	0.5	88.3	81.3	99.1	96.7
Ab	99.2	98.9	8.1	5.6	97.4	99.7	98.8	98.6	98.3	8.7	16.5	0.6	2.3
An	0.0	1.1	0.0	2.4	1.1	0.0	0.5	0.2	1.1	3.0	2.2	0.3	1.1

Table 6.3b. Representative microprobe analyses: Pyroxene

	Budenberri									Tribulation		
	alteration									Metamorphic		
	Bud.g	Bud.g	Bud.g	Bud42	Bud42	Bud42	Bud67	Bud67	Bud67	T58	T58	T58
SiO2%	55.93	53.97	54.69	52.75	54.66	54.89	56.09	55.26	56.71	51.88	51.35	52.98
TiO2%	0.00	0.00	0.09	0.00	0.00	0.04	0.07	0.00	0.00	0.00	0.10	0.00
Al2O3%	0.83	0.47	0.60	0.00	0.24	0.28	0.46	0.13	0.31	1.68	1.65	0.95
FeO%	7.91	7.50	11.40	9.80	8.36	8.78	7.98	8.64	7.28	10.99	12.23	10.37
MnO%	0.00	0.29	0.24	0.40	0.31	0.23	0.00	0.00	0.02	0.59	0.87	0.65
MgO%	12.97	12.72	11.46	12.17	12.10	12.51	12.38	12.93	13.24	10.09	10.42	11.28
CaO%	21.84	22.05	21.09	22.48	23.42	23.50	21.75	21.47	22.20	23.11	23.12	23.27
Na2O%	1.33	2.66	1.97	0.52	0.73	1.33	1.73	1.89	1.55	0.26	0.55	0.73
K2O%	0.19	0.02	0.04	0.00	0.00	0.04	0.00	0.00	0.03	0.03	0.24	0.00
TOTAL%	101.00	99.68	101.58	98.12	99.82	101.60	100.46	100.32	101.34	98.63	100.53	100.23
Atomic Formula Units (afu)												
Si	2.05	2.02	2.03	2.02	2.04	2.02	2.06	2.05	2.06	1.99	1.95	2.00
Ti	0.00	0.00	0.00	0.00	0.00	0.00	0.00	0.00	0.00	0.00	0.00	0.00
Al	0.04	0.02	0.03	0.00	0.01	0.01	0.02	0.01	0.01	0.08	0.07	0.04
Fe	0.24	0.23	0.35	0.31	0.26	0.27	0.25	0.27	0.22	0.35	0.39	0.33
Mn	0.00	0.01	0.01	0.01	0.01	0.01	0.00	0.00	0.00	0.02	0.03	0.02
Mg	0.71	0.71	0.63	0.69	0.67	0.69	0.68	0.71	0.72	0.58	0.59	0.63
Ca	0.86	0.88	0.84	0.92	0.94	0.93	0.86	0.85	0.86	0.95	0.94	0.94
Na	0.09	0.19	0.14	0.04	0.05	0.09	0.12	0.14	0.11	0.02	0.04	0.05
K	0.01	0.00	0.00	0.00	0.00	0.00	0.00	0.00	0.00	0.00	0.01	0.00
Total	3.99	4.07	4.03	4.00	3.98	4.02	3.99	4.02	3.99	3.98	4.03	4.01
XMg	0.75	0.75	0.64	0.69	0.72	0.72	0.73	0.73	0.76	0.62	0.60	0.66
Di	74.5	75.1	64.2	68.9	72.1	71.8	73.4	72.7	76.4	62.1	60.3	66.0
Hed	25.5	24.9	35.8	31.1	27.9	28.2	26.6	27.3	23.6	37.9	39.7	34.0

Table 6.3c. Representative microprobe analyses: Amphibole

	Gilded Rose		Roxmere-Marimo		Camel Hill		Mt Avarice		Budenberri		Tribulation			
	1307	1351a	1384b	1808	1561b	1561b	1375.04	1375.06	Bud42	Bud67	T72c	T72e	T58	T58
SiO2%	53.61	56.07	54.90	54.76	54.54	54.65	56.67	52.81	56.23	53.16	54.22	54.90	40.73	43.51
TiO2%	0.41	0.23	0.25	0.04	0.00	0.10	0.16	0.04	0.00	0.19	0.00	0.19	0.60	0.59
Al2O3%	1.54	1.41	1.73	0.32	1.95	0.04	1.48	2.87	0.84	2.48	1.14	1.76	12.03	9.54
FeO%	9.25	7.64	8.24	8.61	7.25	22.61	9.02	15.45	11.00	8.14	8.64	7.82	19.60	17.12
MnO%	0.28	0.20	0.20	0.24	0.34	1.23	0.36	0.19	0.23	0.00	0.11	0.00	0.32	0.65
MgO%	16.95	19.14	18.00	18.06	18.33	9.73	18.20	14.18	16.46	17.66	17.97	18.62	9.03	10.05
CaO%	11.25	11.50	11.67	11.65	11.43	2.73	12.20	11.92	11.91	11.96	10.36	12.18	11.98	11.97
Na2O%	0.90	0.55	1.46	1.09	1.34	5.46	0.72	0.51	1.42	1.24	1.32	0.62	0.80	0.00
K2O%	0.41	0.20	0.32	0.12	0.53	0.02	0.44	0.37	0.19	0.36	0.49	0.17	2.59	1.91
Cl %	0.09	0.06	0.10	0.06	0.13	0.07	0.10	0.22	0.00	0.07	0.09	0.06	1.02	0.56
TOTAL%	94.70	96.99	96.87	94.96	95.85	96.64	99.34	98.56	98.29	95.25	94.35	96.31	98.69	95.90
Atomic Formula Units (afu)														
Si	7.84	7.91	7.81	7.96	7.80	8.00	7.88	7.63	7.97	7.70	7.90	7.81	6.18	6.67
Ti	0.05	0.02	0.03	0.00	0.00	0.01	0.02	0.00	0.00	0.02	0.00	0.02	0.07	0.07
Al	0.27	0.23	0.29	0.05	0.33	0.01	0.24	0.49	0.14	0.42	0.20	0.30	2.15	1.72
Fe3+	0.09	0.01	0.15	0.06	0.18	1.46	0.05	0.19	0.05	0.14	0.17	0.11	0.78	0.43
Fe2+	1.04	0.89	0.83	0.98	0.68	1.31	1.00	1.68	1.25	0.85	0.88	0.82	1.71	1.76
Mn	0.03	0.02	0.02	0.03	0.04	0.15	0.04	0.02	0.03	0.00	0.01	0.00	0.04	0.08
Mg	3.70	4.02	3.82	3.91	3.91	2.12	3.77	3.06	3.48	3.81	3.90	3.95	2.04	2.30
Ca	1.76	1.74	1.78	1.81	1.75	0.43	1.82	1.85	1.81	1.86	1.62	1.86	1.95	1.97
Na	0.26	0.15	0.40	0.31	0.37	1.55	0.19	0.14	0.39	0.35	0.37	0.17	0.24	0.00
K	0.08	0.04	0.06	0.02	0.10	0.00	0.08	0.07	0.03	0.07	0.09	0.03	0.50	0.37
Total	15.11	15.04	15.18	15.15	15.17	15.04	15.09	15.13	15.15	15.21	15.15	15.07	15.66	15.37
Cl	0.02	0.01	0.02	0.01	0.03	0.02	0.02	0.05	0.00	0.02	0.02	0.01	0.27	0.15
OH	1.98	1.99	1.98	1.99	1.97	1.98	1.98	1.95	2.00	1.98	1.98	1.99	1.73	1.85
XMg	0.77	0.81	0.82	0.79	0.84	0.59	0.78	0.64	0.73	0.82	0.81	0.83	0.54	0.55
log(Cl/OH)	-1.95	-2.14	-1.91	-2.13	-1.79	-2.04	-1.92	-1.56		-2.06	-1.95	-2.14	-0.81	-1.10

Table 6.3d. Representative microprobe analyses: Biotite

	Cloncurry region					Mt Avarice		Roxmere-Marimo		Ernest Henry		Tribulation		
	metamorphic					alt.	infill	alteration		alteration		metamorphic		infill
	0038	0135	1735	1785	0494	1375.04	1375.04	1686c	1714	EH10	EH10	T58	T58	T72h
SiO2%	43.48	39.18	36.75	36.53	39.56	39.48	39.70	40.28	39.73	38.33	41.08	38.59	38.23	43.28
TiO2%	1.00	2.22	2.84	2.48	1.51	2.53	0.21	2.23	1.86	0.87	1.08	1.77	1.66	0.53
Al2O3%	14.02	13.66	13.61	16.20	13.05	11.91	13.16	12.14	11.48	11.41	11.94	13.12	13.57	11.86
FeO%	8.08	11.25	18.30	17.62	15.77	14.67	12.96	17.32	16.77	18.93	13.14	15.52	15.87	11.30
MnO%	0.00	0.00	0.19	0.00	0.00	0.16	0.01	0.02	0.00	0.59	0.58	0.40	0.58	0.00
MgO%	20.06	17.24	13.42	10.88	15.69	15.94	18.24	14.87	15.74	17.75	18.00	14.50	15.36	19.12
CaO%	0.16	0.33	0.29	0.45	0.06	0.26	0.03	0.00	0.16	0.25	0.14	0.00	0.18	0.32
Na2O%	0.24	0.00	0.18	0.00	0.00	0.00	0.00	0.23	0.09	0.00	0.00	0.00	0.14	0.09
K2O%	10.55	10.65	10.59	10.32	10.36	10.23	10.52	10.77	10.25	7.63	9.90	10.21	9.65	10.68
Cl%	0.32	0.28	0.57	0.14	0.76	1.19	0.71	0.39	0.38	0.35	0.36	0.48	0.39	0.24
TOTAL%	97.92	94.79	96.73	94.62	96.75	96.35	95.55	98.26	96.44	96.09	96.22	94.58	95.62	97.41
Atomic Formula Units (afu)														
Si	6.09	5.82	5.59	5.60	5.89	5.92	5.91	5.94	5.95	5.77	6.04	5.88	5.76	6.20
Ti	0.11	0.25	0.33	0.29	0.17	0.29	0.02	0.25	0.21	0.10	0.12	0.20	0.19	0.06
Al	2.31	2.39	2.44	2.93	2.29	2.10	2.31	2.11	2.03	2.03	2.07	2.35	2.41	2.00
Fe	0.95	1.40	2.33	2.26	1.96	1.84	1.61	2.14	2.10	2.38	1.62	1.98	2.00	1.35
Mn	0.00	0.00	0.02	0.00	0.00	0.02	0.00	0.00	0.00	0.08	0.07	0.05	0.07	0.00
Mg	4.19	3.82	3.05	2.49	3.48	3.56	4.05	3.27	3.52	3.99	3.94	3.29	3.45	4.08
Ca	0.02	0.05	0.05	0.07	0.01	0.04	0.00	0.00	0.03	0.04	0.02	0.00	0.03	0.05
Na	0.07	0.00	0.05	0.00	0.00	0.00	0.00	0.07	0.03	0.00	0.00	0.00	0.04	0.03
K	1.89	2.02	2.06	2.02	1.97	1.96	2.00	2.03	1.96	1.47	1.86	1.98	1.85	1.95
Total	15.62	15.75	15.92	15.66	15.78	15.72	15.91	15.80	15.82	15.85	15.74	15.74	15.80	15.73
Cl	0.08	0.07	0.15	0.04	0.19	0.30	0.18	0.10	0.10	0.09	0.09	0.12	0.10	0.06
OH	3.92	3.93	3.85	3.96	3.81	3.70	3.82	3.90	3.90	3.91	3.91	3.88	3.90	3.94
XMg	0.82	0.73	0.57	0.52	0.64	0.66	0.72	0.60	0.63	0.63	0.71	0.62	0.63	0.75
log(Cl/OH)	-1.71	-1.75	-1.42	-2.04	-1.30	-1.09	-1.33	-1.60	-1.61	-1.64	-1.64	-1.50	-1.59	-1.83

Table 6.4. Biotite-Cl chemistry

	Cloncurry Region					Mt Angelay		
	metamorphic					igneous		
	135	0038	0494	1735	1785	Foliated felsic granitoids	Mafic granitoids	Unfoliated felsic granitoids
n=	24	15	16	18	24	14	20	4
XMg (mean)	0.71	0.74	0.63	0.54	0.48	0.69	0.61	0.36
Standard Deviation	0.01	0.02	0.01	0.01	0.08	0.01	0.04	0.03
log(XCl/XOH) (mean)	-1.67	-1.57	-1.27	-1.47	-2.16	-1.70	-1.43	-1.41
Standard Deviation	0.12	0.08	0.03	0.09	0.18	0.09	0.11	0.09
Temperature range (C)	450-550	450-550	450-550	450-550	450-550	590-740	690-760	415-730
Calculation T (C)	500	500	500	500	500	665	725	572.5
log(aH2O/aHCl)	3.33	3.21	2.99	3.25	3.99	3.20	2.92	3.11

	Lightning Cr.	Mt Avarice		Roxmere-Marimo		Ernest Henry	Tribulation	
	alteration	alteration	infill	alteration		alteration	infill	metamorphic
	Qtz monzo-diorite	1375.04	1375.04	1686	1714	EH10	T72h	T58
n=	4	13	6	23	20	22	20	11
XMg (mean)	0.61	0.64	0.70	0.60	0.60	0.65	0.73	0.60
Standard Deviation	0.02	0.01	0.05	0.04	0.01	0.04	0.01	0.01
log(XCl/XOH)	-1.57	-1.12	-1.33	-1.75	-1.81	-1.54	-1.96	-1.52
Standard Deviation	0.16	0.04	0.10	0.16	0.11	0.10	0.04	0.08
Temperature range (C)	600-700	400-600	400-600	400-600	400-600	400-600	400-600	550-650
Calculation T (C)	650	500	500	500	500	500	500	600
log(aH2O/aHCl)	3.13	2.83	3.00	3.49	3.55	3.24	3.61	3.14

Table 6.5. Average magnetite mineral chemistry

		Gilded Rose					Mt Avarice		Roxmere-Marimo	
		Transitional breccias				Ironstone	Na-(Ca) vein (Corella)	Multistage vein (Dolerite)	Na-(Ca) alteration	Na-(Ca) vein
		1307	1310a	1314	1351a	1356a	1375.04	1375.06	1686	1714
	n=	9	4	8	2	5	4	4	8	8
Ti	Mean	161.1	320.0	151.2	135.5	21.2	94.6	741.3	323.0	828.4
	S.D.	58.0	178.0	79.5	26.9	25.4	34.7	153.2	177.5	495.9
V	Mean	1159.4	1491.6	718.3	700.2	530.8	1421.9	2442.1	394.1	2674.6
	S.D.	138.0	231.6	148.2	2.8	13.6	140.7	317.8	38.0	366.2
Mn	Mean	160.0	201.3	131.4	159.9	451.2	506.2	363.4	92.4	81.7
	S.D.	86.1	33.9	32.3	74.3	48.5	59.4	37.3	3.6	21.7
Co	Mean	57.2	58.7	50.5	44.8	58.4	62.4	29.5	24.6	15.4
	S.D.	11.2	12.0	6.1	5.3	0.7	3.2	12.7	0.9	2.2
Ni	Mean	138.7	97.3	91.5	97.5	85.3	70.7	5.7	69.2	108.6
	S.D.	14.1	38.3	7.1	12.1	5.7	13.8	1.4	5.0	60.6
Zn	Mean	19.8	16.2	25.5	10.5	29.5	21.6	41.6	9.9	10.6
	S.D.	9.1	1.6	22.2	1.1	4.7	6.3	12.3	3.4	2.5
Ga	Mean	45.9	39.7	23.1	18.5	13.8	16.7	33.4	14.5	6.4
	S.D.	8.2	11.1	2.0	0.3	0.9	2.0	3.5	2.0	2.4

		Cloncurry region			MKFB	Mt Angelay		Ernest Henry	
		Retrograde breccia	Metamorphic		Transitional breccia	Magmatic-hydrothermal		Ore breccia infill	Mmbx alteration
		0345	1735	1785	MP011d	MA02	MA03	EH09	EH10
	n=	1	4	4	2	4	4	9	3
Ti	Mean	141.3	120.4	82.7	455.9	231.1	753.4	291.4	424.4
	S.D.		19.5	38.5	19.2	223.0	516.2	62.8	52.5
V	Mean	1226.4	809.3	1043.6	3373.9	2364.7	1564.8	500.7	446.2
	S.D.		70.1	178.8	365.0	269.0	84.1	35.7	60.8
Mn	Mean	53.7	366.9	318.3	56.1	194.8	207.6	4598.6	1178.9
	S.D.		40.3	54.7	13.6	41.8	17.0	999.6	290.7
Co	Mean	49.8	41.0	64.3	28.0	29.7	6.1	4.9	9.8
	S.D.		3.7	4.8	11.6	16.4	2.6	2.4	1.5
Ni	Mean	372.0	99.6	89.6	143.6	34.2	24.8	159.4	17.9
	S.D.		11.4	5.0	2.3	10.5	6.4	33.0	1.3
Zn	Mean	5.5	8.1	33.2	4.0	87.0	18.7	32.4	27.2
	S.D.		7.9	12.0	1.1	150.0	5.1	2.6	2.1
Ga	Mean	76.0	8.9	29.2	45.7	16.4	9.5	25.8	13.6
	S.D.		0.8	8.2	2.1	16.2	4.0	3.0	2.1

All values in ppm notation.